submitted to *Geophys. J. Int.*

The role of along-strike variations in interface rheology on subduction dynamics: constraints from 3D numerical models

Derek Neuharth[1,2], Whitney Behr[1], Adam F. Holt[3]

[1] *Geological institute, ETH Zurich, Zurich, Switzerland*

[2] *GFZ German Research Centre for Geosciences, Potsdam, Germany*

[3] *Rosenstiel School of Marine and Atmospheric Science, University of Miami, US*

2025 December

SUMMARY

The strength of the subduction interface plays a major role in controlling subduction dynamics on both local and global scales. While previous studies have primarily examined interface strength in two-dimensional models, natural subduction zones are inherently three-dimensional, with interface strength varying along-strike due to spatial differences in factors such as sediment input. Here, we use the geodynamic code ASPECT to conduct fully dynamic 3D subduction models in which interface strength varies along-strike. We find that the interaction between strong and weak segments of the interface leads to a narrower range of convergence velocities while broadening the range of viable interface stresses compared to 2D or homogeneous 3D models. Stronger segments, when adjacent to weaker ones, exhibit increased convergence velocities. This promotes higher interface stresses and facilitates the subduction of otherwise stagnant strong segments. We find that the interface viscosity of the strong segment controls the baseline stress, whereas the viscosity contrast along-strike controls the magnitude of amplification of the stress due to velocity increases. The elevated interface stresses at strong segments also generate greater compressional forces in the overriding plate than expected from 2D models. Combined with along-strike variations in convergence veloc-

ity, this results in trench migration, with stronger segments displaying more advanced trench positions relative to weaker segments. Possible natural analogs include the Bolivian Orocline in the central Andes and the Lesser Antilles, both of which show enhanced overriding plate compression and trench advance in areas of reduced sediment supply.

Key words: Subduction zone processes, Rheology: crust and lithosphere, Dynamics of lithosphere and mantle

1 INTRODUCTION

The subduction of negatively buoyant lithosphere is fundamental to plate tectonics, driving plate motions, arc volcanism, crustal recycling, and hazardous megathrust earthquakes. Much of our understanding of subduction dynamics comes from geological and geophysical observations and foundational 2D modeling studies, which have provided fundamental insights into processes such as slab rollback, mantle flow, and subduction zone deformation (e.g., Zhong and Gurnis, 1995; Toth and Gurnis, 1998; Conrad and Hager, 1999; Doglioni et al., 2007; Stern, 2002). However, 2D models inherently simplify the system, omitting the along-strike variations now recognized as critical for understanding natural subduction systems. Such variations include differences in subducting plate age, thickness, and slab dip (e.g., Nazca; Cahill and Isacks, 1992; Kay and Mpodozis, 2002; Capitanio et al., 2011), and laterally limited features such as oceanic plateaus (e.g., van Hunen et al., 2002; Liu et al., 2010), mid-ocean ridges (e.g., Bradley et al., 2003), or microcontinental fragments (e.g., van den Broek and Gaina, 2020). These heterogeneities strongly influence subduction dynamics, affecting trench location, curvature, slab dip, and the compressional forces driving mountain building across the convergent margin (e.g., Rodríguez-González et al., 2012, 2016; Balázs and Gerya, 2024; Capitanio et al., 2011).

Another key factor that can vary both with depth and along strike is the mechanical nature of the subduction interface— the weak shear zone that forms between the subducting and overriding plates. This interface can be composed of a variety of materials, including lenses of mafic oceanic crust, ultramafic mantle slivers, and sediments of diverse composition and thickness (Bebout, 2007; Clift and Vannucchi, 2004; Underwood, 2007; Agard et al., 2018). Its bulk frictional

and viscous properties depend on the relative abundances and spatial distributions of different rock types (e.g., Behr and Platt, 2013; Tokle et al., 2023; Zhang et al., 2006; Abila et al., 2024; Ioannidi et al., 2021; Stoner et al., 2025), and on weakening processes such as elevated pore fluid pressures (e.g., Underwood, 2007; Saffer and Tobin, 2011; Sun et al., 2020), shear heating (Peacock, 1996), and/or grain size reduction (Riedel and Karato, 1997; Ruh et al., 2024; Fisher and Hirth, 2024). Interface rheology thus varies dramatically with depth (e.g., due to dehydration reactions and phase transitions with increasing pressure and temperature) and along strike (e.g., owing to variable sediment supply or the subduction of dominantly mafic volcanic features such as ridges or plateaus). Since interface rheology controls shear stress along the subduction interface, it strongly influences convergence velocity and deformation in the overriding plate. While 2D modelling studies have investigated the effect of interface rheology (e.g., Erdős et al., 2021; Behr et al., 2022), and numerous 3D effects have been modeled (e.g., Schellart et al., 2007; Capitanio et al., 2011; Cerpa et al., 2021), no study has explicitly explored the influence of spatially variable interface strengths in dynamically evolving 3D subduction models.

Sediments, in particular, strongly affect interface viscosity and shear stress due to their inherent rheologic weakness relative to mafic oceanic crust (Lamb and Davis, 2003; Behr and Becker, 2018; Tokle et al., 2023; Zhang and Green, 2007). This weakness arises from both their mineralogical composition— dominated by relatively weak quartz and phyllosilicates compared to the stronger minerals that compose mafic rocks— and their ability to promote high pore fluid pressures and the formation of metasomatic weak zones during compaction and dehydration (e.g., Hirauchi et al., 2016; Bebout and Barton, 2002). Although the range of permissible shear stresses for subduction is thought to be relatively narrow (e.g., Lamb and Davis, 2003; Lamb, 2006; Duarte et al., 2015; Schellart, 2024; Abila et al., 2024), variations within this range due to sediment effects can nonetheless have significant impacts on plate dynamics (Behr et al., 2022; Pusok et al., 2022; Abila et al., 2024; Brizzi et al., 2021). For example, changes in convergence velocity driven by sediment subduction have been proposed at both the regional (e.g., India-Eurasia collision, Behr and Becker, 2018) and global scales (Sobolev and Brown, 2019).

An additional consequence of sediment-induced weakening is its effect on stress transfer to

the overriding plate from the slab. The degree of stress transmitted— and hence the extent and type of overriding plate deformation— is closely linked to the shear stress along the interface, with higher interface shear stresses typically correlating with greater compressional stresses (e.g., Lamb, 2006; Dielforder et al., 2020). In systems where sediment input reduces the interface viscosity, the associated drop in shear stress is likely to lead to diminished stress transfer, and in turn, less compressional deformation of the overriding plate. This effect can be large enough to promote back-arc extension (Erdős et al., 2021). Conversely, when the interface is dominated by a mafic composition with a viscosity on the order of, e.g., 10^{21} Pa·s, higher shear stresses can accumulate, leading to greater stress transfer into the overriding plate, and hence elevating overriding plate compressional deformation (e.g., Lamb and Davis, 2003) or potentially even stalling subduction (Behr et al., 2022). While a multitude of factors impact the overriding plate deformation (e.g., plateau subduction, Liu et al. 2010; trench curvature, Cerpa et al. 2021; or plate ages, Capitanio et al. 2011), natural examples such as the Andes and Lesser Antilles also highlight how along-strike variations in sediment input and effective interface properties may lead to localized differences in overriding plate topography and compressional stress state. For instance, in the Andes, in conjunction with an extensive trench length (e.g., Schellart, 2024) and along-strike changes in plate thicknesses (Capitanio et al., 2011), decreases in sediment supply along the Bolivian Altiplano region relative to regions along-strike has been suggested to produce localized regions of high interface shear stress that contribute to uplift (Lamb and Davis, 2003; Hu et al., 2021). Along the Lesser Antilles subduction zone, the northern and southern segments have undergone different tectonic evolutions since the Eocene (e.g., Cerpa et al., 2021; Philippon et al., 2020; Montheil et al., 2023) that may also relate to variations in subducted sediment. During the Eocene, the development of a southward-thickening accretionary wedge (Bangs et al., 2003) coincided with a transition from compression in the north to extension in the southern Grenada Basin (e.g., Cerpa et al., 2021). This phase was subsequently followed by northern extension during the Oligocene (Cerpa et al., 2021). While these cases assume variation in sediment within the subduction channel along-strike, we acknowledge that the ratio of sediment accumulation within an accretionary wedge compared to the input into the interface is not straightforward (e.g., Lallemand et al., 2024).

Regardless, such natural examples highlight the need for modeling approaches that can incorporate along-strike variations in interface rheology as a proxy for varying sediment input.

To systematically explore these effects, we employ fully-dynamic 3D subduction models to investigate how along-strike changes in interface rheology affect subduction zone dynamics. Our models use a constant viscosity interface that is varied from 10^{19} Pa·s, representing a weak sediment-rich interface, to 10^{20} Pa·s or 10^{21} Pa·s, representing variably mafic interfaces. We examine how along-strike changes in interface viscosity, the spatial arrangement of weak versus strong regions, and the length of the overriding plate influence convergence velocity, trench location, overriding plate topography and stress regime.

2 METHODS

2.1 Governing equations

We use the finite-element code Advanced Solver for Problems in Earth's ConvecTion (ASPECT, version 2.5.0-pre; Heister et al., 2017; Kronbichler et al., 2012; Rose et al., 2017; Bangerth et al., 2019) to simulate 3D and time-dependent subduction in the presence of along-strike variations in interface strength. ASPECT solves the following conservation equations assuming the Boussinesq approximation with no inertial term or internal heating.

$$-\nabla \cdot (2\eta \cdot \dot{\varepsilon}) + \nabla P = \rho g \tag{1}$$

$$\nabla \cdot (u) = 0 \tag{2}$$

$$\rho \cdot C_p \left(\frac{\partial T}{\partial t} + u \cdot \nabla T \right) - \nabla \cdot k \nabla T = 0 \tag{3}$$

$$\frac{\partial c_i}{\partial t} + u \cdot \nabla c_i = 0 \tag{4}$$

Equation 1 is the conservation of momentum, with the effective viscosity, η, the deviator of the strain rate tensor, $\dot{\varepsilon}$ (defined as $\frac{1}{2}(\nabla u + \nabla u^T)$, the velocity, u, the pressure, P, the density, ρ, and gravity, g. Equation 2 describes the conservation of mass in an incompressible system. Equation 3 represents the conservation of energy with the specific heat capacity, C_p, the temperature, T. and

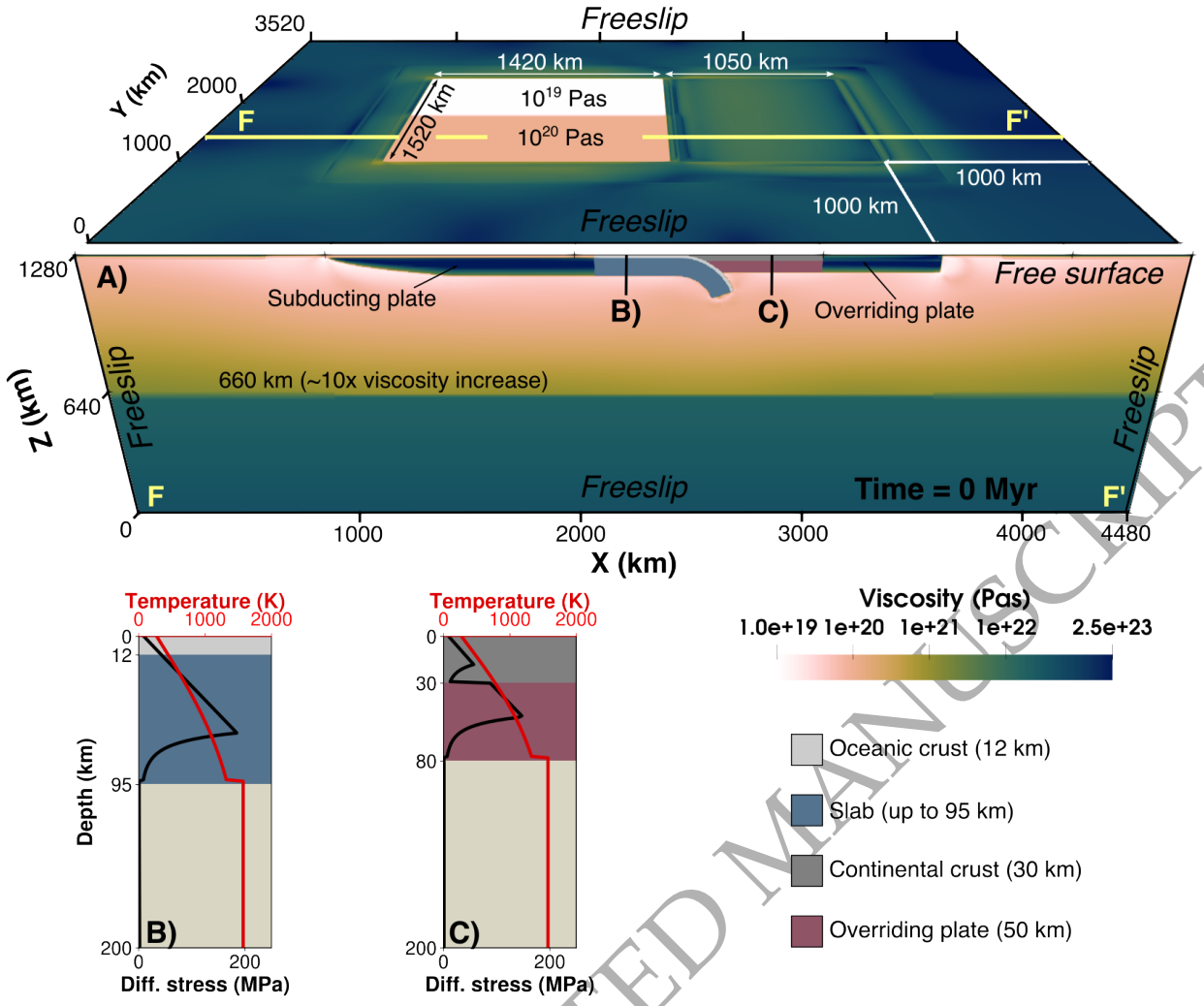

Figure 1. Model setup for case with along-strike variation in interface viscosity. A) shows the surface overlying a slice taken from F to F', colored by viscosity and composition. B) and C) show strength and temperature profiles of the subducting and overriding plate, respectively.

the thermal conductivity, k. Finally, we solve the advection equation 4 for each compositional field c_i.

2.2 Rheology

The models have a viscoplastic rheology (Glerum et al., 2018) that includes viscous and plastic deformation without strain weakening. We use solely dislocation creep for the wet quartzite upper crust of the overriding, continental plate (Tokle et al., 2019). All other compositions including the background material, slab, and oceanic crust deform based on a composite olivine flow-law with

dislocation and diffusion creep (Hirth and Kohlstedt, 2003). Both diffusion and dislocation creep flow laws are given as:

$$\eta^{diff|disl} = \frac{1}{2} A_{diff|disl}^{-\frac{1}{n}} d^{m} \dot{\varepsilon}_e^{\frac{1-n}{n}} exp(\frac{E_{diff|disl} + PV_{diff|disl}}{nRT}) \tag{5}$$

with the scalar prefactor, A, the grain size, d, the second invariant of the deviatoric strain rate, $\dot{\varepsilon}_e$, the activation energy, E, the pressure, P, the activation volume, V, the gas constant, R, the temperature, T, and the stress exponent, n. For diffusion creep, n = 1 and there is no strain rate dependence. For dislocation creep, the grain size exponent, m, is 0 and so it is independent of grain size. Values for A, E, V, and n used in our models are composition-dependent and based on experiments (supplementary Table S1). The scalar prefactor for background material is set to give $\eta^{diff} = \eta^{disl} = 4 \cdot 10^{20}$ Pa·s at a depth of 330 km and a transition strain rate of $5 \cdot 10^{-15} s^{-1}$ (cf. Billen and Hirth, 2005). The effective viscosity is computed as a harmonic average of the dislocation and diffusion creep viscosity above the 660-km transition. We set the lower mantle to deform solely via diffusion creep (Karato and Wu, 1993).

For plastic parameters we use the Drucker-Prager yield criterion (Davis and Selvadurai, 2002) with a friction angle of 5° and cohesion of 10 MPa within all compositions. These values were chosen to approximate the yield stresses associated with the Byerlee Law implementation in Behr et al. (2022) for comparability. The Drucker-Prager yield stress is then computed as:

$$\sigma_y = \frac{6Ccos\phi}{\sqrt{3}(3 - sin\phi)} + \frac{6Psin\phi}{\sqrt{3}(3 - sin\phi)} \tag{6}$$

where C is the cohesion and ϕ the internal angle of friction. The effective viscosity is determined by whether viscous stresses exceed plastic stresses; where this occurs, viscosity is determined by the following equation.

$$\eta_{eff} = \frac{\sigma_y}{2\dot{\varepsilon}_e} \tag{7}$$

Alternatively, in regions where viscous stress are below the plastic yield stress, the effective viscosity is a harmonic average of the dislocation and diffusion creep viscosities:

$$\eta_{eff} = \frac{\eta_{diff} * \eta_{disl}}{\eta_{diff} + \eta_{disl}} \tag{8}$$

2.3 Model setup

We designed thermo-mechanical subduction models using ASPECT that are similar to recent 2-D (Holt and Condit, 2021; Behr et al., 2022) and 3-D models (Turino and Holt, 2024). Here, we adopt the 3-D approach. We use a box geometry with dimensions of 4480 (X), 3520 (Y), and 1280 km (Z; Fig. 1). The top and bottom boundaries are set to fixed temperatures of 273 and 1573 K, respectively. All the side boundaries are set as insulating. All mechanical boundaries are free-slip, except at the model surface, which is implemented as a free surface with an additional diffusion component (1.6 m^2/yr) for mesh stability (e.g., Pons et al., 2022; Grima and Becker, 2024).

2.3.1 Model initial conditions

The model contains distinct overriding and subducting plates, as defined by half-space cooling thermal profiles corresponding to ages of 55 Myr and 80 Myr, respectively (thermal diffusivity of 10^{-6} m^2/s). The uppermost 30 km of the overriding plate represents the upper crust and is compositional buoyant with a reduced reference density (3000 kg/m^3 relative to 3300 kg/m^3 for the background/mantle material). On the subducting plate, the top 12 km represents the interface, parameterized as a generic viscous crustal/metasedimentary layer that is slightly compositionally buoyant (3175 kg/m^3) and set to a constant viscosity (10^{20} Pa·s) until a depth of ∼175 km, where it transitions into background material (e.g., Behr et al., 2022). The chosen interface density lies between typical values for compacted sediments (2700–2800 kg/m^3) and HP–UHP metasedimentary rocks (3100–3400 kg/m^3; e.g., Massonne et al., 2007), and thus implicitly averages over the moderate densification expected as subducted sediments undergo progressive metamorphism, which we do not model explicitly.

Initially, the edges of both the overriding and subducting plates are 1000 km from the model

sidewall boundaries, allowing toroidal flow around the sides of the slab (Fig. 1; e.g., Dvorkin et al., 1993; Funiciello et al., 2003; Kincaid and Griffiths, 2003; Stegman et al., 2010). At the surface, the plates are 1520 km wide along-strike and 1050 and 1420 km in across-strike length for the OP and slab, respectively. At the start of the model, subduction is initiated by allowing an initial portion of the slab, or proto-slab, to extend to a depth of 200 km with a 245 km radius of curvature. Between x = 1500 and 1000 km, the 80 Ma subducting plate thins to zero age to represent a mid-ocean ridge. On all sides, surrounding the plates is a 50 km (in depth and width) weak zone differentiated by a reduced friction angle and cohesion (4° and 5 MPa, respectively). This setup facilitates self-consistent subduction initiation due to the negative buoyancy of the proto-slab and the decoupling of the subducting plate from the surround thermal boundary layer by the weak trailing edge (ridge) and sides (weak zones). At a depth of 660-km, we impose a 10x increase in the diffusion creep viscosity in order to represent the transition into the lower mantle; however, due to the lack of dislocation creep in the lower mantle, the effective viscosity increase can range from ∼10-50x, broadly inline with geoid constraints (e.g., Hager, 1984). In models with along-strike variations in interface strength, the weak vs. strong compositions linearly transition from one to another over 50 km along-strike. Larger transition lengths of 150 and 450 km were tested, however they did not significantly affect the results (supplementary Fig. S1).

2.3.2 Model resolution and walltime

Model resolution varies through time due to ASPECT's adaptive mesh refinement (AMR) functionality and is set to be spatially and compositionally dependent. Our AMR settings result in a maximum resolution of 5 km that is confined to the interface at depths less than 175 km. The overriding plate has a fixed resolution of 10 km, and the slab resolution varies from 10 to 20 km. To resolve plate edges, a temperature isosurface of 1225-1335 K is fixed to a 10 km resolution. The remainder of the model can vary in resolution from 80 to 20 km. Models had $\sim$ 150 million degrees of freedom ($\sim$ 1.4 millions cells) and were run on the ETH Euler cluster; on 512 cores (AMD EPYC 9654) and with ASPECT's GMG solver (Clevenger and Heister, 2021), they had walltimes between 4 and 70 hours, depending on the interface viscosity.

2.4 Model analysis

We ran 15 models to investigate the effects of along-strike changes in interface strength (Fig. 2). Subduction interfaces can consist of multiple different rheologies from weak sediment (e.g., Vrolijk, 1990; Tobin and Saffer, 2009) to strong mafic material, leading to a wide range of probable bulk viscosities (Behr and Becker, 2018). To account for this variation, we use constant viscosity interfaces of either 10^{19}, 10^{20}, or 10^{21} Pa·s. Our reference cases have homogeneous interfaces at these viscosities (section 3.1). These models are compared to cases where there is an along-strike split of the interface into a weak and a strong half (e.g., Fig. 1), which are similarly varied between viscosities of 10^{19} to 10^{21} Pa·s (section 3.2). Section 3.3 investigates the along-strike location of the interface change, with a stripe of weak or strong interface instead placed in the center of the subducting plate. Finally, in section 3.4, we change the trench-perpendicular length of the overriding plate to explore the effect of the overriding plate width-to-length aspect ratio.

In analyzing the models, we focus on 6 model output parameters: 1) convergence velocity, 2) average interface stress, 3) overriding plate compressional forces, 4) area of overriding plate with a thrust faulting regime, 5) overriding plate rotation, and 6) along-strike differences in trench location. To analyze these parameters we extract and analyze 2D trench-perpendicular model slices up to 20 Myr of model time. As the location of the along-strike change in interface rheology may shift both between the model runs, slices are taken an along-strike distance of $\sim$250 km from the change to ensure consistent comparisons. Velocities are averaged over constant 15-km depth profiles. Overriding plate forces, thrust faulting area, and interface stress are determined within the OP or interface, respectively, with the former two being integrated over the plate thickness and from the start of the overriding plate up to 500 km into it; this limit is set to avoid including values at the trailing edge of the plate that are not related to trench dynamics. In calculating the OP forces, we only include trench-perpendicular compressional forces greater than 1 MPa; overall, this analysis method gives us a general idea of the net OP compressional force without constraining where deformation would be focused or whether other areas of the plate may be extensional (see supplementary text S1 for more details). The faulting regime is determined using a discontinuous stress

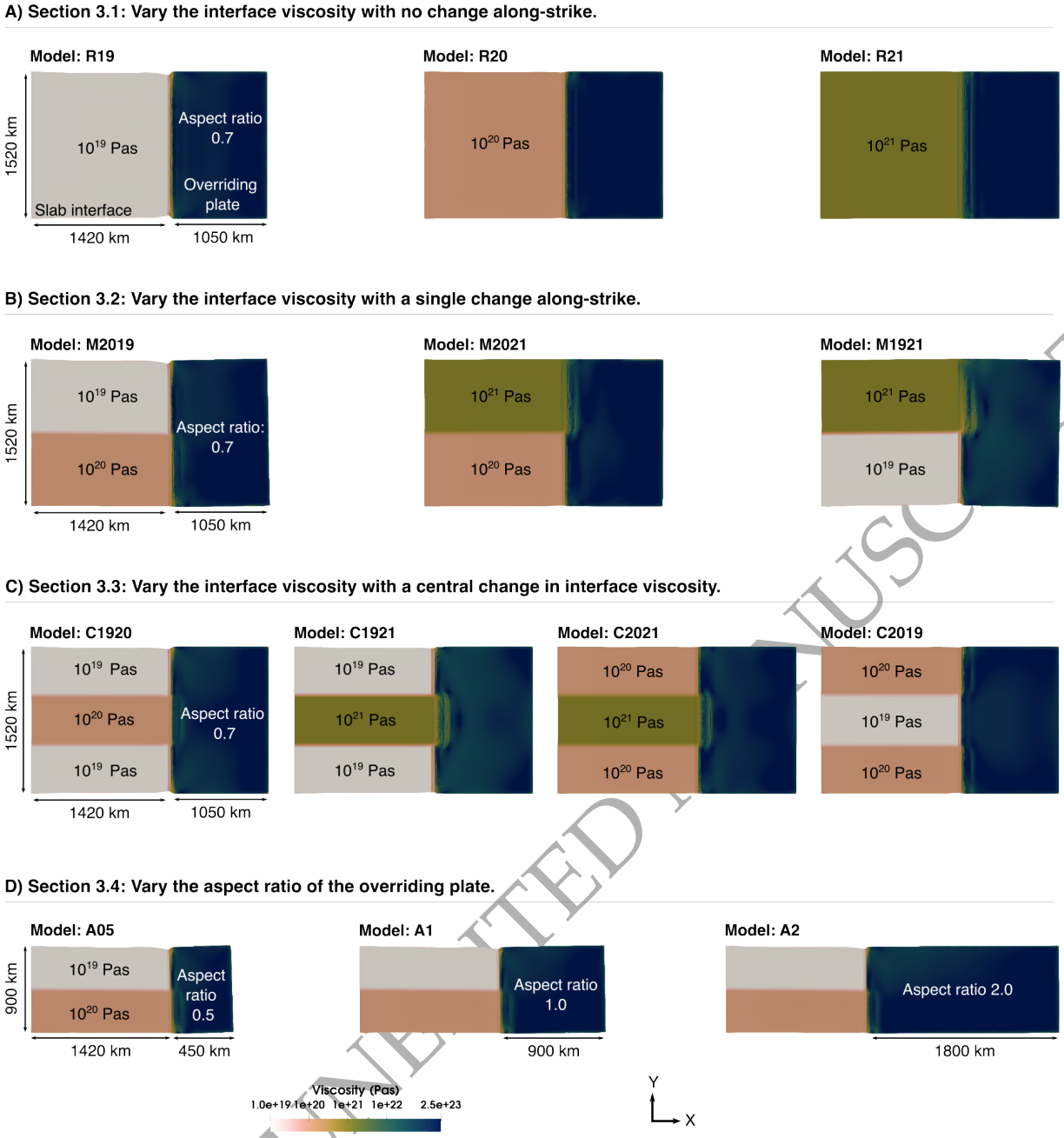

Figure 2. List of models by section to show the initial setup and what is varied, colored by the viscosity. Models are visualized through a composition contour, showing only the slab interface and overriding plate at the surface at 0.5 Myr. Models are given a letter by section. For A)-C), model name numbers are assigned by the interface viscosity. For D), model numbers are assigned according to the overriding plate aspect ratio.

state based on the compressive principal stresses (Zoback, 1992), although we do not consider transitional or strike-slip regimes.

3 RESULTS

3.1 Homogeneous models

3.1.1 Reference homogeneous model evolution

To investigate effects of along–strike changes in interface strength, we first ran three reference models with homogeneous interface viscosities of 10^{19}, 10^{20}, and 10^{21} Pa·s (models R19, R20, and R21). Here, we describe the evolution of model R20 using three trench-perpendicular slices (Fig. 3; supplementary video 1). The model evolution follows three distinct phases: 1) build up to peak convergence velocity (free-sinking phase), 2) decrease in velocity as the slab interacts with the 660-km mantle viscosity increase, and 3) post-660 km slab interaction (cf. Funiciello et al., 2003, 2006).

During the first phase, the model has a low convergence velocity (~3 cm/yr) that increases through time as more plate subducts and the slab lengthens (Fig. 3a). The overriding plate experiences its highest trenchward velocity at the start of the model run before gradually slowing (supplementary Fig. S2). Thrust faulting within the overriding plate is widespread during this stage, with an affected area of ~9250 km^2 along a 2D slice (Fig. 3d), predominantly focused near the plate boundary. As subduction continues, the convergence velocity reaches a maximum of 7.2 cm/yr at ~6 Myr. The average interface stress (Fig. 3b) and compressional force (Fig. 3c) within the overriding plate increase in tandem but reach their peak values (26 MPa and 3.2 TN/m, respectively) slightly earlier, at ~5.5 Myr (Fig. 3g and 3j). Near this time, discrete thrust faults develop in the forearc basin of the overriding plate. By the end of this phase, the slab has reached ~450 km depth and exhibits a convex shape towards the mantle wedge side.

At ~6.5 Myr, the model enters its second phase, where convergence velocity, interface stress, and OP compressional forces begin to decline. While the area of thrust faulting remains large, it starts to decline at a faster rate. As the slab reaches the 660-km transition at ~10 Myr (Fig. 3h and 3k), it undergoes further bending and begins to buckle near the transition to the lower mantle. Around this time, the overriding plate reaches a minimum velocity of ~0.1 cm/yr, coinciding with a pronounced decline in the area of thrust faulting.

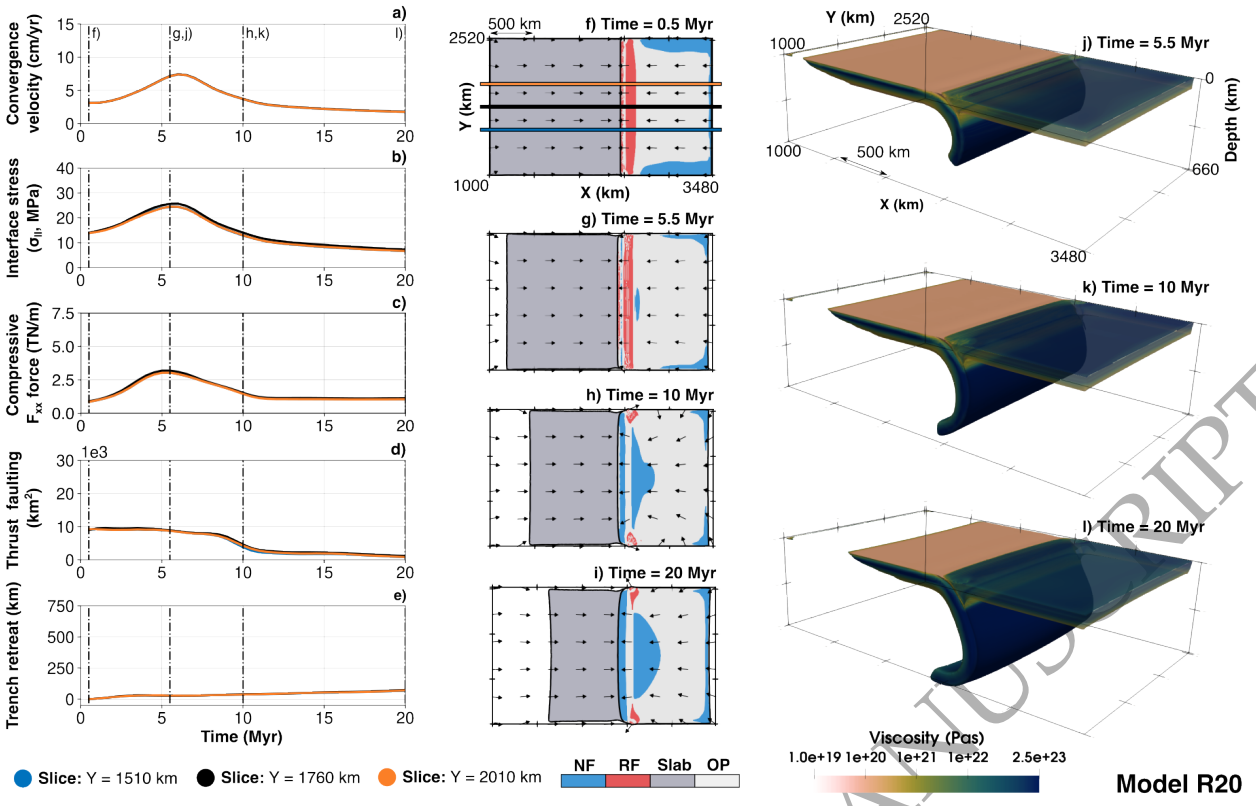

Figure 3. Evolution of the reference 10^{20} Pa·s model without along-strike variations. a)-e) show the time evolution of multiple parameters at different slice locations. f)-i) show a 15-km depth contour colored by composition (dark gray for slab and light gray for overriding plate) and the stress regime based on Zoback (1992) (blue indicates normal faulting and red reverse faulting). Arrows represent velocity direction. j)-l) show a 3D view of the slab and overriding plate colored by viscosity.

In the final phase, following the interaction with the 660-km viscosity transition, slab rollback occurs leading to renewed overriding plate motion and a largely extensional OP faulting regime. During this phase, all of the extracted parameters continue to decline, excluding the OP horizontal compressional forces, which remain relatively constant. We note that trench retreat occurs throughout the model run, and that the slab maintains a similar shape along-strike (Fig. 3l). Within the model, the radius of trench curvature reduces with trench retreat (cf. Schellart, 2010), reaching a minimum of ∼8400 km by 20 Myr.

3.1.2 Homogeneous model comparisons

Before investigating the impact of along-strike variations, we ran two models with constant but distinct interface viscosities of 10^{19} and 10^{21} Pa·s. These models demonstrate a systematic rela-

tionship between interface viscosity and convergence velocity similar to results from previous 2D models (cf. Behr et al., 2022). In the low viscosity 10^{19} Pa·s model (R19), the peak convergence velocity reaches ∼23.6 cm/yr, much greater than the ∼7.5 cm/yr within the 10^{20} Pa·s model (R20) previously described. The greater trench retreat in model R19 also leads to a lower radius of trench curvature (∼3300 km; e.g., Schellart, 2010). In the strongest interface viscosity model of 10^{21} Pa·s (R21), subduction nearly stalls, with a maximum velocity of only ∼0.5 cm/yr. Differences can also be seen in the total trench retreat after 20 Myr of evolution, which range from 620 km in R19 to 75 and 30 km in R20 and R21, respectively.

The maximum of the average OP compressional force is reduced in models R19 and R21 (1.1 and 1.6 TN/m, respectively) relative to the that of R20 (∼3.2 TN/m). Similar to R20, model R19 shows a local peak in the compressional force during the free-sinking phase when convergence velocities reach the maximum (∼1.1 TN/m). However, despite the overall greater convergence velocities in R19 compared to R20 and R21, compressional forces are generally low during the free-sinking phase when convergence velocities are high, and primarily increases late in the run when most of the initial slab has subducted and convergence velocities are low (supplementary Fig. S3). Model R21, likely due to the stalled subduction, has a consistently high value throughout the model run (∼1.5 TN/m).

3.2 Varied interface strength along-strike

To examine the impact of along-strike variations in interface strength, here we introduce models in which the interface viscosity is spatially heterogeneous. These models build upon the homogeneous reference cases by incorporating lateral changes in interface viscosity, allowing us to assess how such variations modify convergence velocity, slab morphology, and overriding plate stress distribution. We begin by describing a reference heterogeneous interface model where the interface viscosity is set to 10^{20} Pa·s from y of 1000 to 1735 km, and 10^{19} Pa·s from 1785 to 2520 km (model M2019; Fig. 4). The transition between these two interface properties occurs over a 50 km region in the center of the model, where the composition linearly shifts from that of the strong to that of the weak material.

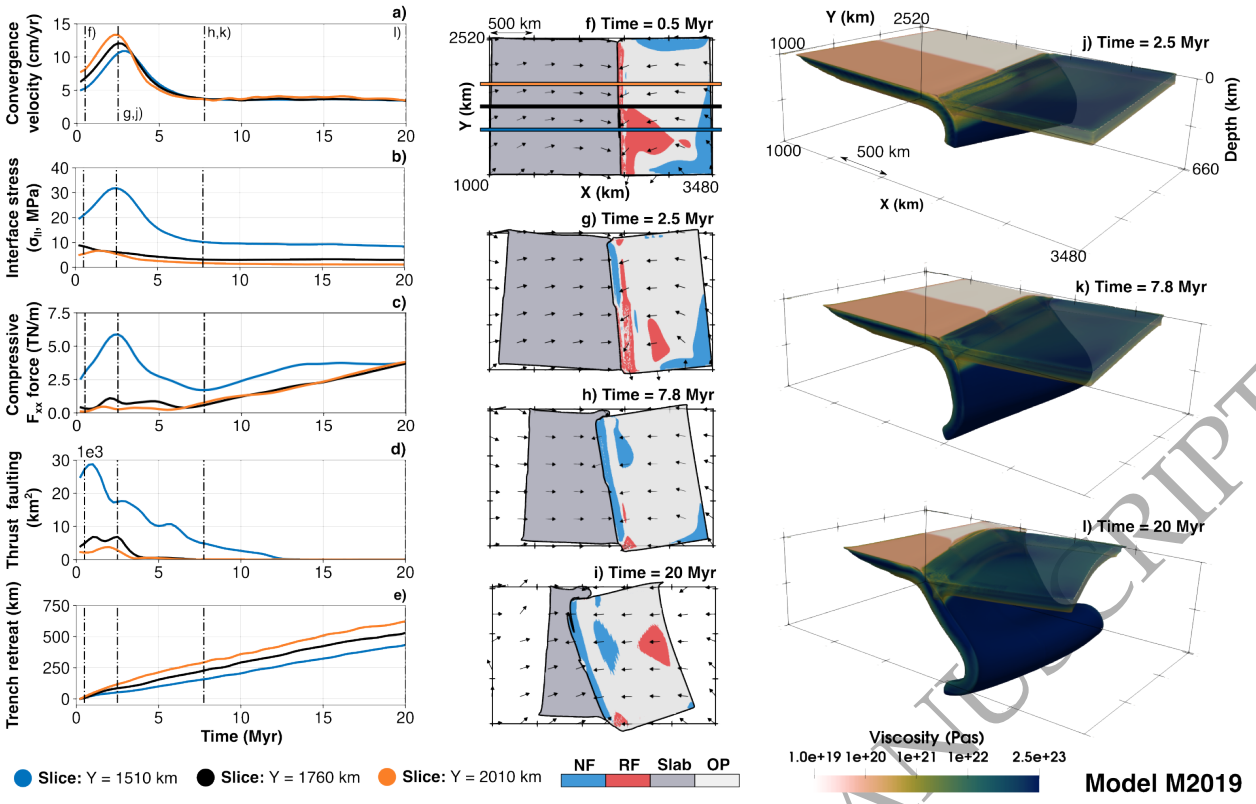

Figure 4. Evolution of the 10^{20} (bottom half) to 10^{19} (top half) Pa·s model without along-strike variations. a)-e) show the time evolution of multiple parameters at different slice locations. f)-i) show a 15-km depth contour colored by composition (dark gray for slab and light gray for overriding plate) and the stress regime based on Zoback (1992) (blue indicates normal faulting and red reverse faulting). Arrows represent velocity direction. j)-l) show a 3D view of the slab and overriding plate colored by viscosity.

3.2.1 Reference varied model evolution

Similar to the reference model without interface strength variations (R20), model M2019 follows three phases: 1) build up to peak velocity, 2) decrease in velocity as the slab reaches the 660-km transition, and 3) post-660 km slab interaction (supplementary video 2). To illustrate the effects of along-strike variations, we analyze slices taken at 250 km to either side of the viscosity transition, allowing for a direct comparison between strong and weak interface segments.

Phase 1: The initial increase in convergence velocity follows that of the homogeneous reference models but exhibits pronounced along-strike differences. On the weak interface side, convergence accelerates rapidly, peaking at 13.4 cm/yr by 2.3 Myr (Fig. 4a). In contrast, the strong interface segment reaches a lower peak velocity of 10.9 cm/yr at 3 Myr. These changes in velocity

can partially be attributed to differences in OP velocity (supplementary Fig. S4), which in these models is broadly equivalent to the trench retreat rate (due to relatively limited OP deformation). This differential trench retreat rate induces a counter-clockwise rotation of the overriding plate and results in a lateral variation in trench position (Fig. 4e). The stress distribution reflects this contrast, with the weak interface section associated with both lower interface stress and lower overriding plate compressional force (Fig. 4b and 4c), while the strong side shows an increase in both properties. By 2.5 Myr, the strong interface segment reaches a peak interface stress of ∼32 MPa and an OP force of ∼5.9 TN/m. This coincides with high variability in the distribution of thrust faulting along-strike, with the strong interface slice showing a thrust faulting regime that extends much farther into the OP (∼17400 km2, Fig. 4d and 4g). During this period of elevated compression, discrete plastic shear zones, mimicking faults, develop near the front of the plate (Fig. 4j). During Phase 1, the radius of trench curvature decreases in both segments, with the strong segment developing a smaller radius. By the end of this phase, there is a ∼65 km along-strike difference in trench position between the two slices, which can be attributed to the OP rotation associated with differential trench retreat rates and overriding plate shortening (Fig. 4g).

Phase 2: At ∼2.5 Myr, the slab segment with the weak interface reaches ∼460 km depth, and the convergence velocity begins to decline. However, the velocity along the strong interface segment continues to increase, peaking slightly later before also beginning to decrease. As velocity decreases, interface stress, the OP force, and the area of thrust faulting begin to subside. By ∼5 Myr, the slab on the weak interface side reaches the 660 km transition and anchors into the stronger lower mantle. This initiates elevated slab rollback on the weak interface side and an associated shift towards an extensional OP. Along the strong interface, the slab has not yet reached 660 km, overriding plate speeds are low, and there is a small peak of thrust faulting in the OP (Fig. 4d). At ∼7.8 Myr (Fig. 4h and 4k), the rest of the slab, in the strong segment, anchors into the lower mantle, coinciding with the minimum OP force on that side of the subduction zone. By this time, because of the difference in trench retreat rate along-strike and slab anchoring on the weak interface side, there is an along-strike variation in slab dip, with the strong interface side

exhibiting a steeper dip (∼53°) that reduces towards the weak interface (∼41°). Throughout Phase 2, the radius of trench curvature continues to decline for both segments.

Phase 3: By 8 Myr, extensional stresses develop along the entirety of the OP, and although the compressional forces in the X direction rise, due to stress orientations the area of thrust faulting reduces to less than ∼100 km^2 by 13 Myr (Fig. 4d). The convergence velocities and average interface stress are near-constant during this phase, and the along-strike change in trench location continues to increase due to continued differential trench retreat rates. By the end of the model run, the weak interface side has retreated 190 km more than at the strong interface and exhibits a 6° shallower dip, leading to a highly variable slab shape along-strike (Fig. 4l). The radius of trench curvature continues to decrease in both segments until 13.5 Myr, at which point the strong segment reaches a minimum of ∼1550 km, compared to ∼1950 km along the weak segment. During subsequent slab rollback, the radius in the strong segment begins to increase as the curvature evolves under the influence of trench retreat rather than OP compression (cf. Schellart, 2010). By the end of the model, the strong and weak segments reach radii of approximately ∼1650 km and ∼1250 km, respectively (radius of trench curvature values for all remaining models are provided in Supplementary Table S2).

3.2.2 Comparison of models with variable segment viscosities

To further investigate the influence of along-strike viscosity changes, we ran two additional models with weak segment viscosities of 10^{19} and 10^{20} Pa·s, and a strong segment viscosity of 10^{21} Pa·s (models M1921 and M2021, respectively). We discuss the models by comparing each segment to its respective homogeneous reference case, as well as assessing the overall along-strike variability.

The first order model evolution of M1921 and M2021 are similar to model M2019. On the weak interface side, both convergence velocities and overriding plate compressional forces are lower than in their corresponding reference homogeneous model (Fig. 5 and Fig. 6). Compared to the stronger side, the weak subduction segments have both higher subduction velocities and greater trench retreat rates, which results in a change in the trench location along-strike and hence rotation of the overriding plate. On the strong interface side, all models show increased OP compressional

forces and convergence velocities relative to their reference homogeneous models (Fig. 5d and 5e; Fig. 6). Notably, while the reference 10^{21} Pa·s model (homogeneous plate interface) experiences stalled subduction (cf. Behr et al., 2022), pairing it with a lower-viscosity segment allows subduction to proceed at low velocities while maintaining elevated overriding plate compressional forces.

The differences between models primarily depend on the magnitude of the viscosity contrast along-strike. While lower along-strike averages of viscosity result in higher convergence velocities overall, the OP compressional forces are sensitive to both the viscosity of the strong segment and the viscosity ratio between segments. For example, in two models with a 10x viscosity increase along-srike (M2019 and M2021), the strong segment of model M2019 (10^{20} Pas) shows higher convergence rates but lower average compressional forces than the strong segment of M2021 (10^{21} Pas, 4.6 vs. 3.3, Fig. 5e), suggesting the importance of the viscosity magnitude. Although both models reach a similar peak compressional force ($\sim$5.6 TN/m), the slab within M2021 takes longer to reach the 660-km viscosity jump (7.8 Myr in M2019 vs. $>$20 Myr in M2021), leading to an extended phase of high OP compression. This effect is even more pronounced in model M1921 where the increased viscosity contrast (20x) relative to M2021 (10x) results in the highest compressional stresses. In this case, the strong interface side in M1921 exhibits both higher average convergence velocities ($\sim$1.5 cm/yr) and greater OP force ($\sim$9.1 TN/m) compared to M2021 ($\sim$1 cm/yr and 4.6 TN/m), indicating that convergence velocity also controls the OP force even if the strong interface viscosity remains constant. These factors collectively contribute to along-strike changes in trench location with strong interfaces associated with trench advance and weak trenches with trench retreat, either through increased overriding plate rotation due to differential trench velocity, or through variations in compressional deformation. We also examined the influence of the amount of weak interface along-strike, which showed that a higher proportion of weak interface further elevated the velocities in the strong segment, but the effect was less pronounced than those explored here (supplementary Fig. S5, text S2).

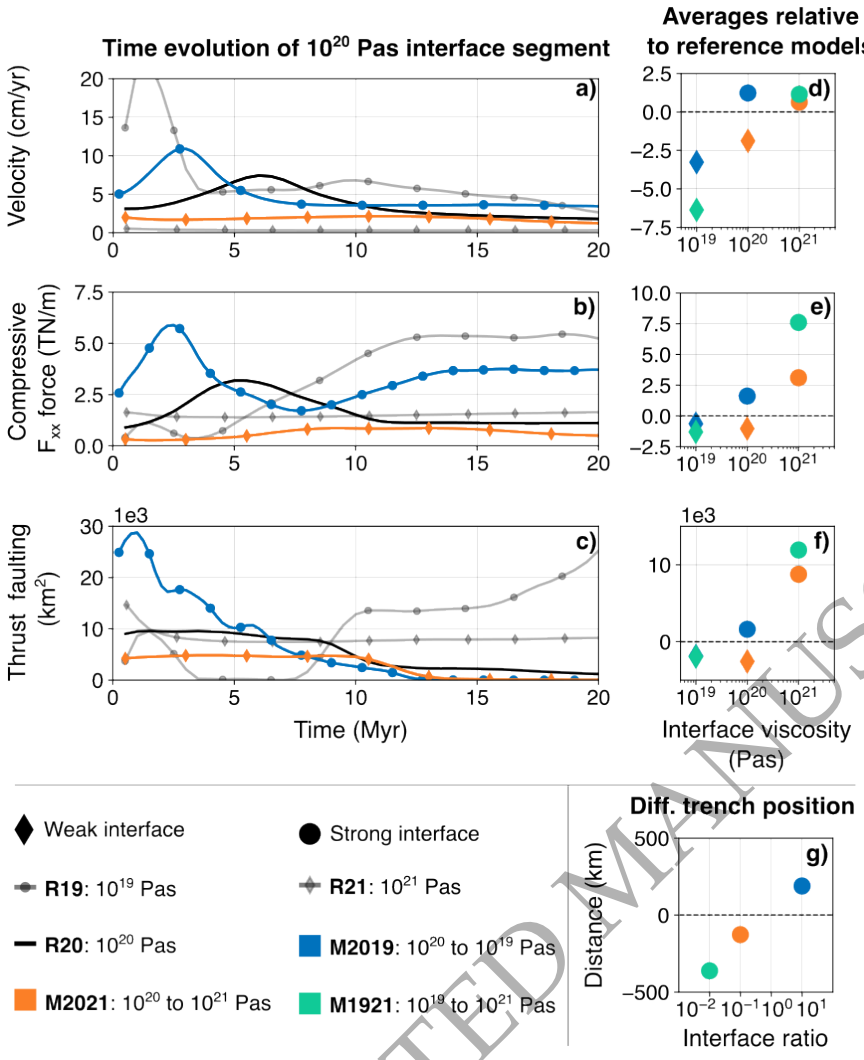

Figure 5. Comparison between models with different interface viscosities along-strike. Symbols indicate whether the model is a slice from the strong or weak interface. Color indicates the model. a)-c) show the time evolution of two models compared to the reference model (black), with both lines indicating the 10^{20} Pa·s model side. d)-e) show the same values time-averaged and scaled to the reference model, and additionally show values corresponding to the 10^{19} and 10^{21} Pa·s sides of the models. g) Indicates the difference in trench location for each model along-strike, where the interface ratio refers to the difference in viscosity from the interface at low Y-values to that at high Y-values (e.g., model M2019 from figure 4 has an interface ratio of 10^{1} because it has a 10^{20} Pa·s interface at lower Y-values and a 10^{19} Pa·s interface at high Y-values) and where a positive value indicates the trench at the front model side is advanced relative to the back.

3.3 Central interface models

While in our previous models we explored a single viscosity contrast along-strike, the relative location of strong vs. weak interface segments may also influence model evolution. To investigate this, we ran four additional models where we split the downgoing plate into thirds, varying the

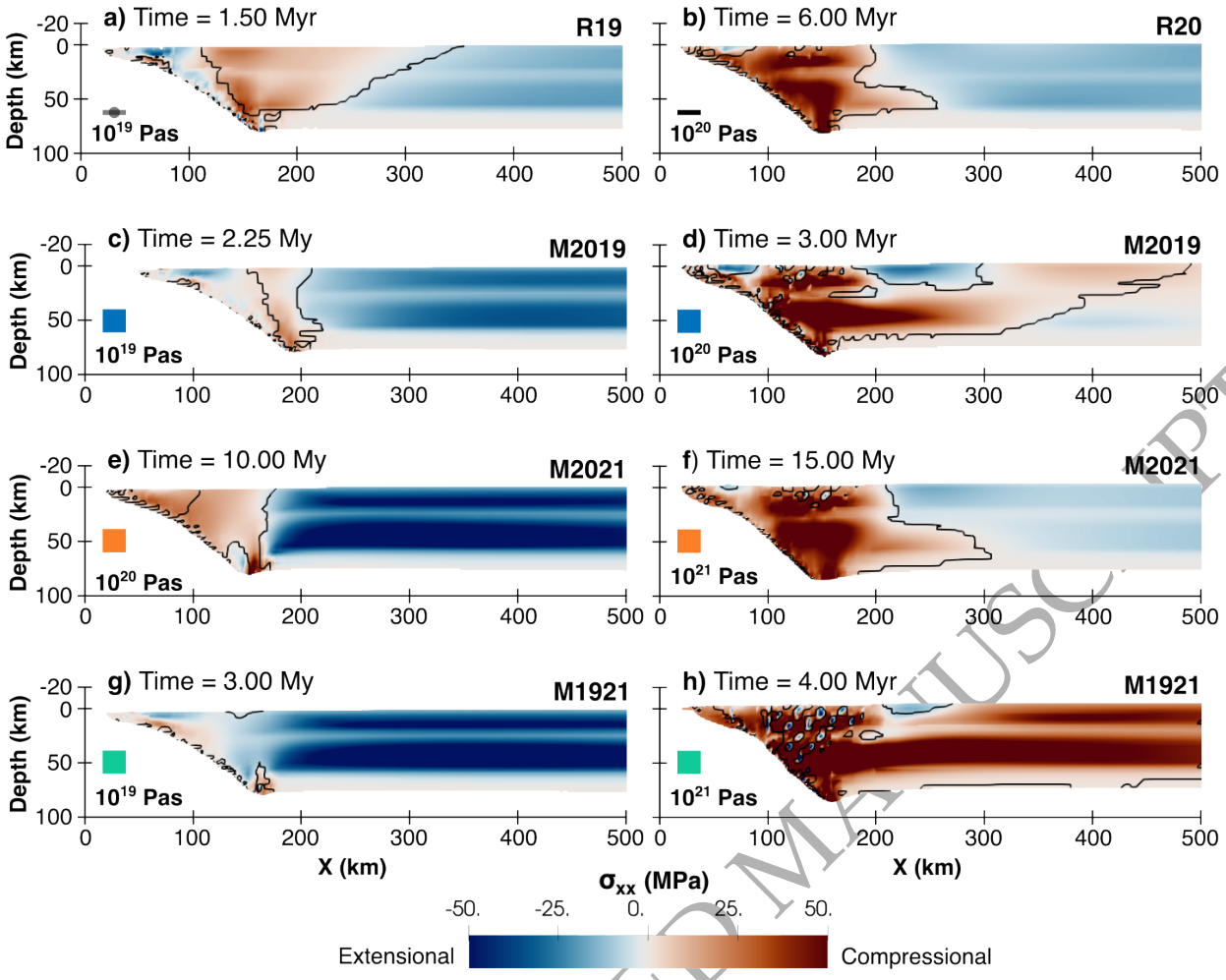

Figure 6. Model slice snapshots of the overriding plates deviatoric stress in X showing the 500 km used in determining the integrated compressive force and area of thrust faulting. Colored boxes indicate the model with respect to Fig. 4. Positive Sxx represents compressive stresses and negative extensive stresses. The black contour shows the region of thrust faulting. Snapshots are taken at the time of max convergence velocity for each slice.

viscosity of the central segment of the interface relative to the outer two segments (model C1920, C1921, C2021, C2019). These models (Fig. 7) are compared to the models from section 3.2 (Fig. 5).

Similar to the models in section 3.2, the central interface models show increased OP forces at strong interface regions and variations in trench position along-strike. The margin geometry appears to take one of two characteristic shapes: 1) a concave profile with an advanced central region when the central interface is strong (Fig. 7e), or 2) a convex profile with a retreated central trench when the central interface is weak. A notable difference between these models and

those in Section 3.2 is less variation in the convergence velocity along-strike. For example, model M2019 exhibits an average along-strike convergence velocity difference between the strong and weak slices of ∼1.2 cm/yr, whereas C2019 exhibits smaller variation of only 0.2 cm/yr (Fig. 7a). Compared to the models in section 3.2, these central models are pinned on either side of the central segment resulting in less OP rotation (Fig. 7b, supplementary video 3) and a greater increase in OP compressional force (Fig. 7c) within the strong interface section. Overall, this results in less pronounced changes in trench location (e.g., 365 and 270 km for M1921 and C1921, respectively).

3.4 Overriding plate aspect ratio

In the previous models, we used a 0.7 aspect ratio of the overriding plate (strike-perpendicular length to along-strike width); however, this ratio is likely to also play a role in overriding plate dynamics due to its impact on the net mantle shear forces, which scale with plate size, acting at the base of the overriding plate. To explore this, we ran three models with an altered geometrical setup, where the model is 4480 x 2400 km in X and Y, with 750 km gaps around the edges of 900 km wide subducting and overriding plates. The trench-perpendicular length of the overriding plate was varied between 450, 900, and 1800 km, corresponding to aspect ratios of 0.5, 1, and 2 (models A05, A1, and A2). These models have an interface viscosity change in the model center from 10^{20} to 10^{19} Pa·s, as in model M2019.

Increasing the overriding plate length and aspect ratio affects the models in several ways. A larger aspect ratio reduces overriding plate rotation (Fig. 8a), approaching no rotation at an aspect ratio of 2. Unlike the models in Section 3.3, the reduction in rotation is accompanied by a reduction in overriding plate compressional force within the strong interface section, from 1.6 TN/m with an aspect ratio of 0.5 to 1.3 TN/m at a ratio of 2 (Fig. 8b). Interestingly, the average convergence velocities on the strong interface side remain relatively unchanged across aspect ratios, with values of 3.6, 3.5, and 3.7 cm/yr for A05, A1, and A2, respectively. However, due to variation in the net basal shear force on the OP, the partitioning between subduction velocity and OP velocity changes (cf. Holt and Becker, 2016): as the aspect ratio increases, subduction velocity increases while OP velocity decreases. This occurs because, for larger OPs, subduction via trench retreat becomes

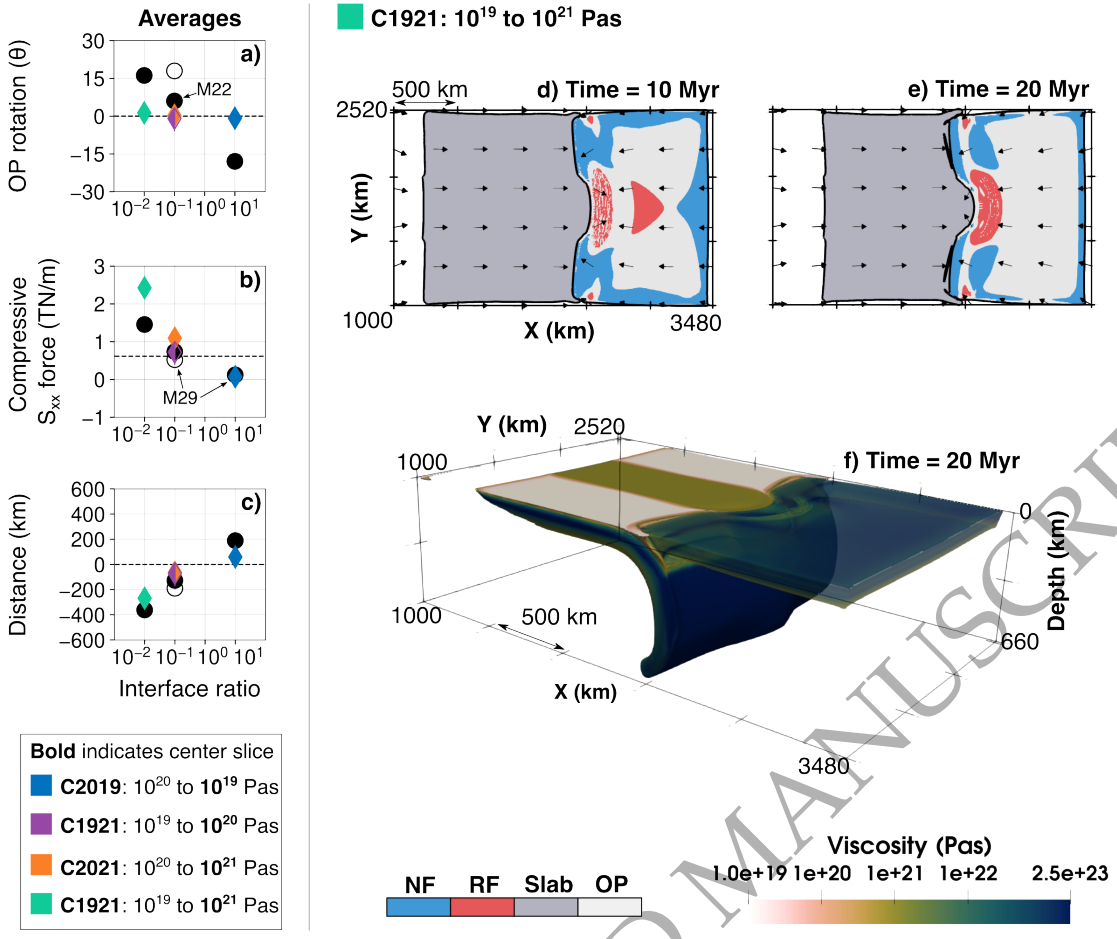

Figure 7. Comparison between models where the change in interface is placed in the center of the model. Symbols indicate whether it is a center model (colored diamond), or a varied model from section 3.2 (black circles). Shape fill is used to better see overlapping symbols. a)-d) Parameters against the along-strike interface viscosity ratio, shown as front to back slice. a) Differential convergence velocity along-strike. b) Total overriding plate rotation by model end. c) Average compressive force in overriding plate. d) Difference in trench location along-strike. Model M2019 is shown twice, with the hollow circle showing the back to front slice. d) Indicates the difference in trench location for each model along-strike where a positive value indicates the trench at the front model side is advanced relative to the back. e)-g) Show snapshots of a single model evolution, see Fig. 2 for explanation.

more difficult (due to increased basal shear resistance associated with OP motion). Compared to model M2019, all the models here exhibit lower OP compressional forces, and reduced convergence velocity on the strong interface (4.8 cm/yr for M2019). As OP rotation and compressional forces decrease with increasing aspect ratio, along-strike trench position variations also become less pronounced. The difference in the trench X-location along-strike between the two slices re-

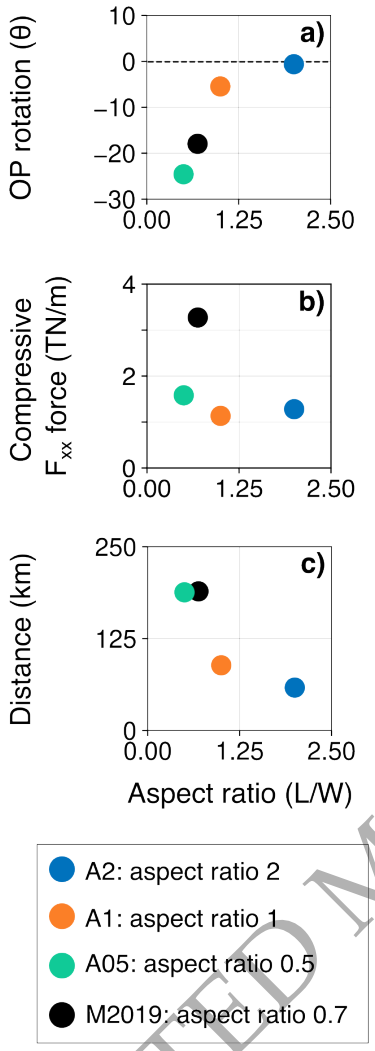

Figure 8. Comparison between models where the length to width aspect ratio of the overriding plate is varied. Color indicates the model, with the black circle representing M2019 from section 3.2. a)-c) Show the a) total overriding plate rotation, b) time-averaged compressive OP force, c) total trench difference between the front and back slice against the aspect overriding plate ratio.

duces from 188 km to 58 km at aspect ratios of 0.5 and 2, respectively (Fig. 8c). This suggests that multiple factors influence trench location, including shortening and the relative balance between overriding and subducting plate basal tractions (and hence velocities). The latter of which affects OP rotation and depends on not only interface strength but also relative plate sizes.

4 DISCUSSION

4.1 Effects of along-strike variations and extrapolation from 2D to 3D

The viscosity of the interface can span 2-3 orders of magnitude depending on the distribution of rock types (e.g., Behr and Becker, 2018; Abila et al., 2024), which itself can vary substantially along-strike (e.g., Lamb and Davis, 2003; Kelemen et al., 2003; MacKay and Moore, 1990). Several 2D numerical modeling studies have shown that interface strength strongly influences subduction dynamics: weak interfaces promote slab rollback, increase convergence velocity, and reduce slab dip which can inhibit slab penetration through the 660-km phase transition (e.g., Conrad and Hager, 1999; Čížková and Bina, 2013, 2019; Behr et al., 2022).

To compare to these results from two-dimensional models, we first examine our homogeneous interface strength (R19, R20, R21) models. Our 3D model results are consistent with the 2D studies: at low interface viscosity (10^{19} Pa·s), convergence rates approach ~24 cm/yr (R19), while at high viscosity (10^{21} Pa·s), subduction almost stalls with velocities below $\sim$ 0.5 cm/yr (R21), in line with the 2D values reported by Behr et al. (2022). We also observe trends in slab geometry that are consistent with earlier work: higher interface strength produces steeper slabs (62° vs. 71° in R19 and R20, respectively; Čížková and Bina, 2013; Behr et al., 2022) and reduced trench retreat/rollback distances within a 20 Myr time interval (620 vs. 70 km in R19 and R20).

When along-strike variations in interface strength are introduced, their effects on convergence rate, slab dip, and rollback interact spatially, leading to more complex subduction dynamics. Our models show that these variations affect both local and plate-scale convergence rates. For example, the homogeneous reference model R20 exhibits a peak convergence rate of 7.5 cm/yr. When paired with a weak interface (M2019), the 10^{20} Pa·s segment velocities increase to 10.9 cm/yr. Conversely, coupling the same 10^{20} Pa·s interface with a stronger rheology (M2021) reduces convergence velocities to 2.1 cm/yr (Fig. 5a). This behavior is particularly interesting in configurations where a very strong interface— such as model R21, which stalls at 0.5 cm/yr when homogeneous— is instead partially accelerated by an adjacent weak interface segment. In the axial-symmetric model shown in Figure 7, the weak interface segments cause the entire subduction

zone to subduct faster relative to the homogeneous R21 model (up to 2.9 cm/yr in model C1921), with only minor variations in convergence velocity along-strike (approximately 0.3 cm/yr). In non axial-symmetric models (e.g., Fig., 4), the slab on the weak interface side subducts faster and penetrates deeper into the mantle. This forms a slab step that increases slab pull along-strike (e.g., Zuhair et al., 2022), and causes the strong interface to subduct faster (up to 2.6 cm/yr in model M1921) than the 0.5 cm/yr convergence rates in the homogeneous R21 case. Faster subduction along the weak interface segment leads to earlier anchoring in the 660-km transition zone, triggering rollback within that section and altering the trench orientation. This along-strike variation in slab behavior driven by differences in dip, rollback rate, convergence velocity, and compressional forces produces complex slab and trench geometries (e.g., Fig. 4l), with strong interface segments exhibiting trench advance relative to weaker ones. These results highlight how along-strike variations in interface rheology can influence subduction dynamics well beyond their local region.

4.2 Interface stress and overriding plate deformation

Overriding plate deformation along subduction margins is primarily driven by 1) normal stresses related to trench motion (e.g., Nakakuki and Mura, 2013; Holt et al., 2015), 2) basal drag (Capitanio et al., 2010; Schellart and Moresi, 2013; Nakakuki and Mura, 2013), and 3) interface shear stress (Lamb and Davis, 2003; Behr et al., 2022; Hu et al., 2021). While all are present in our models, we focus here on the interface shear stress, and specifically the second invariant of deviatoric stress along the interface (as a proxy for interface shear stress which is the main stress component within these models, as shown in supplementary Fig. S6), and how it scales with convergence velocity, interface viscosity and overriding plate deformation regime. In nature, the range of interface shear stresses is not well known and appears to vary over an order of magnitude, depending on both geologic setting and the method or timescale associated with the estimation (e.g., force-balance, Zhong and Gurnis 1994; paleopiezometry, Behr and Platt 2013; heat flow constraints, England 2018). While some studies suggest that low long-term viscous interface shear stresses (e.g., less than 35 MPa) are most consistent with global subduction behavior (e.g., Duarte et al., 2015), oth-

ers propose that higher values are viable, especially in systems with significant topographic loads (e.g., Lamb and Davis, 2003; Lamb, 2006).

Previous geodynamic subduction modelling has shown that strong interface viscosities can lead to high shear stresses that stall subduction (e.g., Behr et al., 2022). This is consistent with our homogeneous interface models; for example, model R21 exhibits an average interface shear stress of 14.6 MPa and undergoes subduction stalling. However, in models that incorporate along-strike variations in interface strength, we observe significantly higher interface stresses than in homogeneous models for equivalent interface strengths, yet subduction still proceeds. This is because, as discussed in Section 4.1, pairing a strong interface segment with a weak segment increases the velocity of the strong side relative to the homogeneous reference case, due to increased slab pull sourced from the deeper, adjacent slab with a weaker interface. This velocity increase results in elevated interface stresses (supplementary Fig. S7), with the magnitude of stress controlled by both the viscosity of the strong segment and the viscosity contrast along strike. For instance, interfaces with 10^{21} Pa·s viscosity on the strong side exhibit the highest average interface stresses (e.g., C2021; up to 43 MPa compared to a maximum of 26 MPa seen in homogeneous models), and larger viscosity contrasts along strike further amplify these stresses (e.g., C1921; up to 56 MPa). Because 2D and homogeneous 3D models cannot capture this interaction, they likely underestimate the range of viable shear stress conditions under natural subduction scenarios. These results suggest that the viscosity of the strong segment controls the baseline stress, while the along-strike viscosity contrast controls how much that stress is amplified, with larger contrasts causing greater velocity increases in the strong segment (e.g., supplementary Fig. S7).

To assess the realism of our modeled stresses and velocities, we compare them with natural subduction zone observations. A global compilation by Schellart and Rawlinson (2013) shows that 86% of subduction segments converge between 2 and 12 cm/yr, a range Duarte et al. (2015) linked to a maximum interface shear stress of ∼35 MPa based on analog modelling. This suggests sustained subduction requires low interface strength, which these authors suggested could be due to fluids and consistently weak materials at the interface. Our models align fairly well with the convergence velocity constraints. Prior to slab anchoring (first 700 km of subduction), 70% of

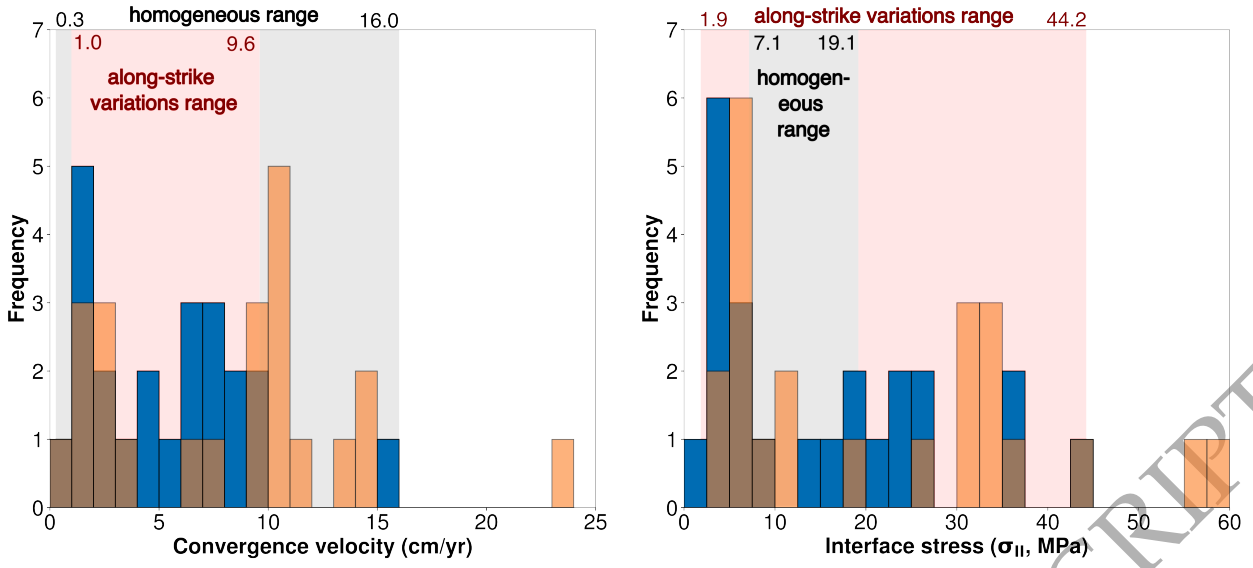

Figure 9. Histograms showing the maximum (orange) and time averaged (blue) values for the a) convergence velocity and b) interface shear stresses. Shaded red regions show the range for the time-averaged models with along-strike variations, and shaded grey shows the range for homogeneous models.

our 23 modeled segments fall within the 2–12 cm/yr range. While slightly lower than natural estimates, this includes 22% of segments with a high interface viscosity (10^{21} Pas) that would cause stalled subduction in homogeneous models. Across our suite, homogeneous models show a broad velocity range (0.3–16 cm/yr time-averaged, 0.5-23.6 cm/yr maximums), but the models with along-strike variations more closely mirror nature (1–9.6 cm/yr time-averaged, 1.1 to 14.4 cm/yr maximums). These variable models simultaneously yield a wider range of interface stresses, with time-averaged values that span 2–44 MPa (58 MPa maximum) compared to 7–19 MPa (23 MPa maximum) in homogeneous models. While only 17% (4 segments) of segments exceed the empirical 35 MPa stress threshold at some point during the model run, three of these maintain convergence rates above 2 cm/yr, indicating that higher interface stresses are viable under certain geometries. Notably, 43% of segments exceed 30 MPa, even with moderate viscosities (10^{20} Pas). These findings show that along-strike variability not only narrows velocity distributions to a more realistic range but also allows a broader range of interface stresses, challenging the assumption that velocity alone can be used to constrain interface strength.

4.2.1 Deformation and topography

High interface shear stresses play a key role in transmitting stress from the negatively buoyant slab and into the overriding plate (OP) (e.g., Lamb, 2006), promoting subduction margin deformation. Figure 10 illustrates a clear relationship between OP compressional force, extracted before slab anchoring, and interface stress, showing an exponential increase in OP force with rising interface stress. As discussed in Section 4.2, homogeneous models yield a relatively narrow range of interface stress, whereas introducing along-strike strength variations significantly expands the range of interface stresses leading to a larger range of compressional forces (0.1 to 15.2 TN/m; Fig. 10).

In addition to interface shear stresses, the exponential relationship observed in Fig. 10 may also result from variations in the normal stresses, as potentially influenced by geometric factors such as slab dip. Slab dip affects the connection between interface and OP stress states: a steeper dip can increase interface normal stresses while reducing shear stresses. However, we note that in our models, high shear stresses persist even at the largest slab dips (e.g., in model C1921, shear and normal interface stresses reach up to 95 and 28 MPa in the strong central segment, respectively, at the time of maximum OP compression). Force balance analysis further suggests that larger slab dips at strong interfaces enhance both the normal component of interface stresses and the horizontal normal stresses transmitted to the overriding plate (Lamb, 2006). When OP forces are normalized by slab dip, the relationship becomes approximately linear (Supplementary Text S3 and Fig. S8), implying that slab dip variations contribute to the elevated OP compression observed at high interface strengths during the free-sinking phase. Strong interfaces also reduce trench retreat (Behr et al., 2022), and in some cases, promote a transition to trench advance, further enhancing compressional deformation in the overriding plate (Capitanio et al., 2010; Holt et al., 2015; Pons et al., 2022; Schellart, 2024). We note that basal drag is another important component to consider for subduction dynamics (e.g., Suchoy et al., 2021; Cerpa et al., 2022) and the OP force balance (e.g., Schellart and Moresi, 2013), with trench-perpendicular gradients in basal traction shown to correlate with OP stress regime (e.g., Capitanio et al., 2010; Schellart and Moresi, 2013), particularly in the far-field. However, in this study we primarily focus on OP deformation in the near-forearc region and on the impact of interface-stress transmission, which we expect

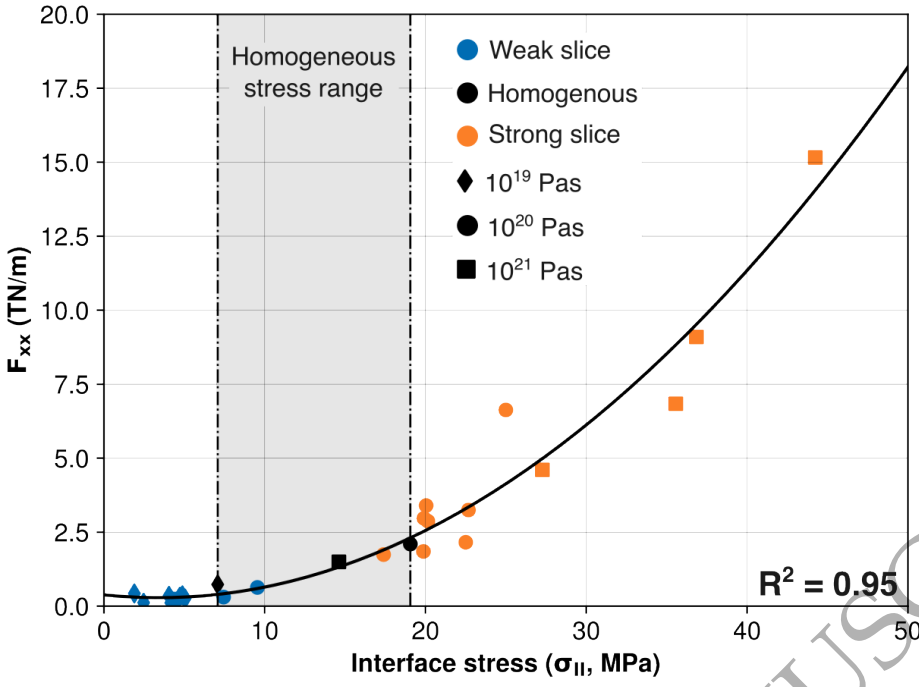

Figure 10. Time-averaged compressive overriding plate force vs. interface stress, from initiation (200-km) to 700-km of subduction.

to dominate adjacent to the plate interface. Analyses of subduction transects suggests back-arc compression occurs primarily above relatively low slab dips (Lallemand et al., 2005), and that the stress regime of the overriding plate following slab anchoring depends on temporal variations in slab dip (Cerpa et al., 2018). More research is required to better understand the interplay between slab dip and the normal and shear stresses along the interface, how this varies along-strike within 3D subduction zones containing variable interface lithologies, and how this relates overriding plate stress state and deformation

Our results indicate that overriding plate deformation is significantly influenced by along-strike variations in slab pull forces, which arise from interface strength heterogeneities. Homogeneous models, by neglecting these variations, tend to underestimate both interface shear stresses and overriding plate forces. In contrast, incorporating along-strike heterogeneity reveals forces up to ~7 times higher, suggesting a more prominent role for these variations in controlling overriding plate dynamics than previously recognized.

4.2.2 Topography

Subduction zone and overriding plate topography varies based on a variety of factors such as the slab dip, buoyancy, and plate strengths (Crameri et al., 2017), as well as overriding plate heterogeneity (Grima and Becker, 2024). Here, we focus on the interface stress magnitude which is also thought to impact topography, affecting trench depth and maximum elevation of the overriding plate (Lamb, 2006; Dielforder et al., 2020). In our models, we see that trench depths correlate positively with interface stresses, ranging from 1.6 to 5.5 km (Fig. 11a). Maximum elevations similarly increase with higher stresses (Fig. 11b) but less dramatically than anticipated by analytical studies (e.g., up to ∼4 km for a ∼50 MPa 80-km thick constant stress interface Dielforder et al., 2020). This lower-than-expected topography may result from limited model resolution (10 km in the OP) and an absence of plastic strain weakening, both of which restrict the development of faults that would drive uplift. Nonetheless, strong interfaces clearly produce greater cumulative relief variations (3.6 to 13.4 km, Fig. 11c), correlating with deeper forearc basins and highs. Although compressional forces typically promote surface uplift, the slab's downward pull in strongly coupled, strong interface regions can counteract this effect and suppress topography (e.g., Behr et al., 2022). Our strong interface models show increased relief and deeper forearc basins, consistent with features like the Atacama Bench in the Andes (Armijo et al., 2015). Our results also suggest that after slab anchoring, when the slab becomes supported by the lower mantle, uplift occurs in the forearc basin. These findings highlight the need for further study on how along-strike variations in interface strength influence sediment transport and deposition from the forearc to the trench.

4.3 Trench location and natural comparisons

A key observation from our models is that along-strike variations in interface strength significantly influence trench location and slab shape. Such variability in subduction geometry is commonly observed in nature, e.g., within the Andes and Lesser Antilles subduction zones. In our simulations, strong interfaces limit slab roll back and increase OP compression, resulting in steeper slab dips and advanced trench positions. When a strong interface region is centrally located, it produces

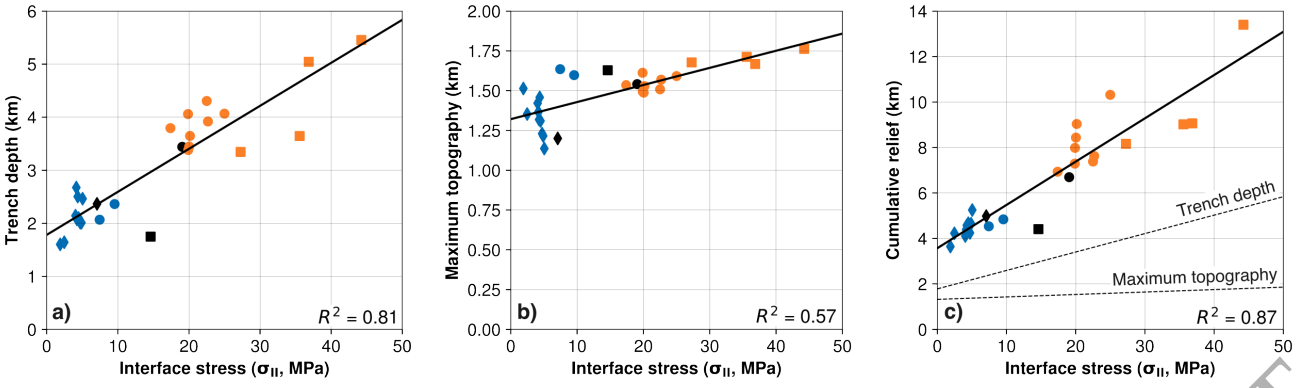

Figure 11. Time-averaged interface stress vs. time-averaged a) trench depth, b) maximum topography, and c) cumulative relief. Cumulative relief is the integration of topographic changes from the trench to 500 km towards the direction of subduction. For information on symbols and colors, see Fig. 10.

concave margin geometries (e.g., model C1921 or C1920, Fig. 7 and supplementary Fig., S9). A natural analog to this configuration is potentially the Bolivian Orocline in the Andes, characterized by an advanced trench with substantial overriding plate deformation. Previous research has attributed this geometry partially to elevated shear stresses resulting from reduced sediment supply (Lamb and Davis, 2003; Hu et al., 2021), although trench length, plate thickness, and slab dynamics may also significantly contribute to such configurations. Shorter subduction zones typically exhibit convex trench geometries towards the subducting plate (e.g., Fig. 3), while longer subduction margins, exceeding several thousand kilometers, often develop concave shapes (Schellart, 2024). Additionally, along-strike variations in the thickness of the subducting and overriding plates influence trench migration and curvature: thicker subducting plates promote rollback and enhance OP compressional stresses, yielding concave shapes when centrally positioned (Capitanio et al., 2011). Conversely, thicker overriding plates tend to reduce trench migration, causing convex trench geometries (Capitanio et al., 2011). The Andean margin, extending approximately 7400 km, exhibits notable along-strike variations in subducting plate age (Lamb and Davis, 2003; Capitanio et al., 2011), and sediment availability possibly linked to climatic variations (Lamb and Davis, 2003; Hu et al., 2021). The distinctive concave shape and pronounced deformation along the Bolivian Orocline may arise from a combination of its extensive length, thicker subducting plate (Capitanio et al., 2011) and amplified local stresses due to a stronger interface set up by reduced sedimentation (Lamb and Davis, 2003; Hu et al., 2021).

When strong interfaces are not axially symmetric but instead paired with weaker interfaces along-strike, an S-shaped trench can form as the weak-interface slab retreats (e.g., M2019, M2021, or M1921, Fig. 4 and supplementary Fig. S9). A similar trench morphology is observed in the Lesser Antilles subduction zone in the Caribbean, which during the Eocene experienced shortening, partially due to trench curvature (Cerpa et al., 2021), in the sediment-starved north and extension in the sediment-rich south (Cerpa et al., 2021). This northern compressional phase was followed by forearc extension in the Oligocene (Philippon et al., 2020; Cerpa et al., 2021). In the southern segment, sediment influx from the South American continent that began in the Eocene (Bangs et al., 2003) may have lubricated the subduction interface (e.g., Behr and Becker, 2018), potentially facilitating faster convergence velocities and promoting slab retreat. Following initial lubrication, sustained sediment supply could have supported growth of the accretionary wedge, increasing the interface length. If the interface viscosity remained constant, this increased interface length coupled to reduced slab pull due to sediment buoyancy might have subsequently slowed convergence velocities and slab retreat (Brizzi et al., 2021; Munch et al., 2022; Keum and So, 2021, 2023). Thus, the overall observed velocities and compressive forces along the margin could reflect a dynamic balance among the rates of sediment input to the interface, accretionary wedge accumulation, and northward sediment propagation.

4.4 Model limitations

The models presented here are simplified to remain interpretable and computationally feasible, while still capturing first-order subduction dynamics. However, because of this we neglect multiple factors that can have an impact on evolving subduction systems. For example, in using a constant interface viscosity, we neglect temperature-dependent, power law rheology. Importantly, this means the entire interface exhibits an average, viscous shear stress, whereas in nature one would expect an increase in shear stress with depth until the brittle-ductile transition, producing a shallow region of very high shear stresses to drive fault localization and overriding plate deformation. Similarly, we neglect surface processes, which could introduce weak sediment rheology to the trench and alter interface strength through time (e.g., Behr and Becker, 2018; Sobolev and

Brown, 2019). Additionally, while in our models a weak interface broadly represents a sedimented interface, to reduce model complexity and focus solely on strength we omit the associated interface density variations. Such density changes have been suggested to influence dynamics, trench location and convergence velocities (Keum and So, 2021, 2023; Munch et al., 2022; Brizzi et al., 2021). In large-scale 3D models we are constrained by the model resolution, reaching a maximum of 5 km in the interface or 10 km in the overriding plate. These resolutions can effect minimum shear zone widths and stress transfer rate across the interface (Conrad and Hager, 1999), as such we may underestimate compressional forces within the overriding plate. Our models capture only a single free-sinking phase. However, in nature, multiple episodes of slab sinking may occur due to processes like slab buckling, which is associated with elevated convergence rates and compressional forces (e.g., Ribe, 2003; Lee and King, 2011; Gibert et al., 2012; Cerpa et al., 2014; Pons et al., 2022; van der Wiel et al., 2024). This means that compressional events linked to interface strength variations could occur repeatedly over time, a behavior not captured in our current modeling framework.

5 CONCLUSIONS

In this study, we explored how along-strike changes in plate interface strength affects a time-evolving 3D subduction zone. Our results show that many aspects of subduction zone behavior in our models, such as slab dip, trench location, and overriding plate deformation, are broadly consistent with findings from previous 2D studies. For example, weaker interface segments promote trench retreat, lower slab dips, and extension in the overriding plate. However, our 3D models reveal an important dynamic not captured in 2D or homogeneous setups: slab segments interact laterally, with weak segments driving faster convergence that enhances velocities even in adjacent, stronger segments. This coupling leads to elevated interface shear stresses and increased transfer of compressional stress to the overriding plate within the strong interface regions. Critically, the magnitude of the along-strike variation in interface strength governs the velocity change within a strong segment, while the local interface strength determines the magnitude of stress amplification.

On a broader scale, along-strike variations in interface strength influence subduction dynam-

ics beyond their immediate location. These variations narrow the range of convergence velocities compared to homogeneous models with similar strength end-members, bringing model behavior closer to natural observations. At the same time, they expand the range of viable interface stresses. Natural examples such as the Andean and Lesser Antilles subduction zones may reflect this behavior: both exhibit elevated overriding plate deformation in sediment-starved regions, with trench geometries characterized by locally advanced trenches adjacent to more retreated, sediment-rich segments. In the Lesser Antilles, increased compressional stresses since the Eocene also coincide with accretionary wedge formation. These observations are consistent with our results, which suggest that along-strike strength variations can amplify interface shear stress and overriding plate deformation. This mechanism may be underestimated in earlier models and operates across spatial scales relevant to evolving subduction zones.

ACKNOWLEDGMENTS

The authors would like to thank Nestor Cerpa and an anonymous reviewer for their detailed and constructive feedback on this manuscript. This work was supported by an ERC starting grant (S-SIM, grant #: 947659) awarded to WMB. AFH was partially supported by NSF EAR 2119842. We thank the Computational Infrastructure for Geodynamics (geodynamics.org) which is funded by the National Science Foundation under award EAR-0949446 and EAR-1550901, for supporting the development of ASPECT. Models were run using the ETH Zurich Euler cluster. Figures were created using Paraview, InkScape, and Python using color scales from Crameri (2018).

DATA AVAILABILITY

Files and the specific ASPECT version used to run the models here can be found at `https://doi.org/10.5281/zenodo.16779892`

References

Abila, A. L., Behr, W. M., and Ruh, J. (2024). Strength of viscous subduction interfaces: A global compilation. *Geology*.

Agard, P., Plunder, A., Angiboust, S., Bonnet, G., and Ruh, J. (2018). The subduction plate interface: Rock record and mechanical coupling (from long to short timescales). *Lithos*, 320:537–566.

Armijo, R., Lacassin, R., Coudurier-Curveur, A., and Carrizo, D. (2015). Coupled tectonic evolution of andean orogeny and global climate. *Earth-Science Reviews*, 143:1–35.

Balázs, A. and Gerya, T. (2024). Modelling the contrasting tectonic and magmatic evolution of rifted and transform margins and subsequent oceanic spreading. *Tectonophysics*, 889:230446.

Bangerth, W., Dannberg, J., Gassmoeller, R., and Heister, T. (2019). Aspect v2.1.0. *Zenodo*.

Bangs, N. L., Christeson, G. L., and Shipley, T. H. (2003). Structure of the lesser antilles subduction zone backstop and its role in a large accretionary system. *Journal of Geophysical Research: Solid Earth*, 108(B7).

Bebout, G. E. (2007). Metamorphic chemical geodynamics of subduction zones. *Earth and Planetary Science Letters*, 260(3):373–393.

Bebout, G. E. and Barton, M. D. (2002). Tectonic and metasomatic mixing in a high-t, subduction-zone mélange—insights into the geochemical evolution of the slab–mantle interface. *Chemical Geology*, 187(1-2):79–106.

Behr, W. M. and Becker, T. W. (2018). Sediment control on subduction plate speeds. *Earth and Planetary Science Letters*, 502:166–173.

Behr, W. M., Holt, A. F., Becker, T. W., and Faccenna, C. (2022). The effects of plate interface rheology on subduction kinematics and dynamics. *Geophysical Journal International*, 230(2):796–812.

Behr, W. M. and Platt, J. P. (2013). Rheological evolution of a mediterranean subduction complex. *Journal of Structural Geology*, 54:136–155.

Billen, M. I. and Hirth, G. (2005). Newtonian versus non-newtonian upper mantle viscosity: Implications for subduction initiation. *Geophysical Research Letters*, 32(19).

719 Bradley, D. C., Kusky, T. M., Haeussler, P. J., Goldfarb, R. J., Miller, M. L., Dumoulin, J. A.,
720 Nelson, S. W., and Karl, S. M. (2003). Geologic signature of early tertiary ridge subduction in
721 alaska. *Geology of a transpressional orogen developed during ridge-trench interaction along*
722 *the North Pacific margin*.

723 Brizzi, S., Becker, T. W., Faccenna, C., Behr, W., van Zelst, I., Dal Zilio, L., and van Dinther, Y.
724 (2021). The Role of Sediment Accretion and Buoyancy on Subduction Dynamics and Geometry.
725 *Geophysical Research Letters*, 48(20):e2021GL096266.

726 Cahill, T. and Isacks, B. L. (1992). Seismicity and shape of the subducted Nazca Plate. *Journal*
727 *of Geophysical Research: Solid Earth*, 97(B12):17503–17529.

728 Capitanio, F., Faccenna, C., Zlotnik, S., and Stegman, D. (2011). Subduction dynamics and the
729 origin of andean orogeny and the bolivian orocline. *Nature*, 480(7375):83–86.

730 Capitanio, F. A., Stegman, D. R., Moresi, L.-N., and Sharples, W. (2010). Upper plate controls on
731 deep subduction, trench migrations and deformations at convergent margins. *Tectonophysics*,
732 483(1-2):80–92.

733 Cerpa, N. G., Guillaume, B., and Martinod, J. (2018). The interplay between overriding plate
734 kinematics, slab dip and tectonics. *Geophysical Journal International*, 215(3):1789–1802.

735 Cerpa, N. G., Hassani, R., Arcay, D., Lallemand, S., Garrocq, C., Philippon, M., Cornée, J.-
736 J., Münch, P., Garel, F., Marcaillou, B., et al. (2021). Caribbean plate boundaries control on
737 the tectonic duality in the back-arc of the lesser antilles subduction zone during the eocene.
738 *Tectonics*, 40(11):e2021TC006885.

739 Cerpa, N. G., Hassani, R., Gerbault, M., and Prévost, J.-H. (2014). A fictitious domain method for
740 lithosphere-asthenosphere interaction: Application to periodic slab folding in the upper mantle.
741 *Geochemistry, Geophysics, Geosystems*, 15(5):1852–1877.

742 Cerpa, N. G., Sigloch, K., Garel, F., Heuret, A., Davies, D. R., and Mihalynuk, M. G.
743 (2022). The effect of a weak asthenospheric layer on surface kinematics, subduction dynam-
744 ics and slab morphology in the lower mantle. *Journal of Geophysical Research: Solid Earth*,
745 127(8):e2022JB024494.

746 Čížková, H. and Bina, C. R. (2013). Effects of mantle and subduction-interface rheologies on

slab stagnation and trench rollback. *Earth and Planetary Science Letters*, 379:95–103.

Čížková, H. and Bina, C. R. (2019). Linked influences on slab stagnation: Interplay between lower mantle viscosity structure, phase transitions, and plate coupling. *Earth and Planetary Science Letters*, 509:88–99.

Clevenger, T. C. and Heister, T. (2021). Comparison between algebraic and matrix-free geometric multigrid for a stokes problem on adaptive meshes with variable viscosity. *Numerical Linear Algebra with Applications*, 28(5):e2375.

Clift, P. and Vannucchi, P. (2004). Controls on tectonic accretion versus erosion in subduction zones: Implications for the origin and recycling of the continental crust. *Reviews of Geophysics*, 42(2).

Conrad, C. P. and Hager, B. H. (1999). Effects of plate bending and fault strength at subduction zones on plate dynamics. *Journal of Geophysical Research: Solid Earth*, 104(B8):17551–17571.

Crameri, F. (2018). Scientific colour maps. *Zenodo*, 10:5281.

Crameri, F., Lithgow-Bertelloni, C., and Tackley, P. J. (2017). The dynamical control of subduction parameters on surface topography. *Geochemistry, Geophysics, Geosystems*, 18(4):1661–1687.

Davis, R. O. and Selvadurai, A. (2002). *Plasticity and Geomechanics*. Cambridge University Press.

Dielforder, A., Hetzel, R., and Oncken, O. (2020). Megathrust shear force controls mountain height at convergent plate margins. *Nature*, 582(7811):225–229.

Doglioni, C., Carminati, E., Cuffaro, M., and Scrocca, D. (2007). Subduction kinematics and dynamic constraints. *Earth-Science Reviews*, 83(3):125–175.

Duarte, J. C., Schellart, W. P., and Cruden, A. R. (2015). How weak is the subduction zone interface? *Geophysical Research Letters*, 42(8):2664–2673.

Dvorkin, J., Nur, A., Mavko, G., and Ben-Avraham, Z. (1993). Narrow subducting slabs and the origin of backarc basins. *Tectonophysics*, 227(1-4):63–79.

England, P. (2018). On shear stresses, temperatures, and the maximum magnitudes of earthquakes

775 at convergent plate boundaries. *Journal of Geophysical Research: Solid Earth*, 123(8):7165–
776 7202.

777 Erdős, Z., Huismans, R. S., Faccenna, C., and Wolf, S. G. (2021). The role of subduction interface
778 and upper plate strength on back-arc extension: Application to mediterranean back-arc basins.
779 *Tectonics*, 40(8):e2021TC006795.

780 Fisher, D. M. and Hirth, G. (2024). A pressure solution flow law for the seismogenic zone:
781 Application to Cascadia. *Science Advances*, 10(4):eadi7279.

782 Funiciello, F., Faccenna, C., Giardini, D., and Regenauer-Lieb, K. (2003). Dynamics of retreat-
783 ing slabs: 2. insights from three-dimensional laboratory experiments. *Journal of Geophysical*
784 *Research: Solid Earth*, 108(B4).

785 Funiciello, F., Moroni, M., Piromallo, C., Faccenna, C., Cenedese, A., and Bui, H. A. (2006).
786 Mapping mantle flow during retreating subduction: Laboratory models analyzed by feature
787 tracking. *Journal of Geophysical Research: Solid Earth*, 111(B3).

788 Gibert, G., Gerbault, M., Hassani, R., and Tric, E. (2012). Dependency of slab geometry on
789 absolute velocities and conditions for cyclicity: insights from numerical modelling. *Geophysical*
790 *Journal International*, 189(2):747–760.

791 Glerum, A., Thieulot, C., Fraters, M., Blom, C., and Spakman, W. (2018). Nonlinear viscoplastic-
792 ity in aspect: Benchmarking and applications to subduction. *Solid Earth*, 9:267–294. Viscosity
793 is rescaled. If viscous stress exceeds yield stress, viscosity becomes lower in that region and the
794 stresses remain at the yield stress.

795 Grima, A. G. and Becker, T. W. (2024). The role of continental heterogeneity on the evolution of
796 continental plate margin topography at subduction zones. *Earth and Planetary Science Letters*,
797 642:118856.

798 Hager, B. H. (1984). Subducted slabs and the geoid: Constraints on mantle rheology and flow.
799 *Journal of Geophysical Research: Solid Earth*, 89(B7):6003–6015.

800 Heister, T., Dannberg, J., Gassmöller, R., and Bangerth, W. (2017). High accuracy mantle con-
801 vection simulation through modern numerical methods – ii: Realistic models and problems.
802 *Geophysical Journal International*, 210:833–851.

Hirauchi, K.-i., Fukushima, K., Kido, M., Muto, J., and Okamoto, A. (2016). Reaction-induced rheological weakening enables oceanic plate subduction. *Nature Communications*, 7(1):12550.

Hirth, G. and Kohlstedt, D. (2003). Rheology of the upper mantle and the mantle wedge: A view from the experimentalists. In Eiler, J., editor, *Geophysical Monograph Series*, volume 138, pages 83–105. American Geophysical Union, Washington, D. C.

Holt, A. F., Becker, T., and Buffett, B. (2015). Trench migration and overriding plate stress in dynamic subduction models. *Geophysical Journal International*, 201(1):172–192.

Holt, A. F. and Becker, T. W. (2016). The effect of a power-law mantle viscosity on trench retreat rate. *Geophysical Journal International*, page ggw392.

Holt, A. F. and Condit, C. B. (2021). Slab temperature evolution over the lifetime of a subduction zone. *Geochemistry, Geophysics, Geosystems*, 22(6):e2020GC009476.

Hu, J., Liu, L., and Gurnis, M. (2021). Southward expanding plate coupling due to variation in sediment subduction as a cause of andean growth. *Nature communications*, 12(1):7271.

Ioannidi, P. I., Le Pourhiet, L., Agard, P., Angiboust, S., and Oncken, O. (2021). Effective rheology of a two-phase subduction shear zone: Insights from numerical simple shear experiments and implications for subduction zone interfaces. *Earth and Planetary Science Letters*, 566:116913.

Karato, S. I. and Wu, P. (1993). Rheology of the upper mantle: A synthesis. *Science*, 260:771–778.

Kay, S. M. and Mpodozis, C. (2002). Magmatism as a probe to the neogene shallowing of the nazca plate beneath the modern chilean flat-slab. *Journal of South American Earth Sciences*, 15(1):39–57.

Kelemen, P. B., Yogodzinski, G. M., and Scholl, D. W. (2003). Along-strike variation in the aleutian island arc: Genesis of high mg# andesite and implications for continental crust. *Inside the subduction factory*, 138:223–276.

Keum, J.-Y. and So, B.-D. (2021). Effect of buoyant sediment overlying subducting plates on trench geometry: 3d viscoelastic free subduction modeling. *Geophysical Research Letters*, 48(9):e2021GL093498.

Keum, J.-Y. and So, B.-D. (2023). Sediment buoyancy controls the effective slab pull force and deviatoric stress along trenches: Insights from 3d free-subduction model. *Tectonophysics*, 862:229970.

Kincaid, C. and Griffiths, R. (2003). Laboratory models of the thermal evolution of the mantle during rollback subduction. *Nature*, 425(6953):58–62.

Kronbichler, M., Heister, T., and Bangerth, W. (2012). High accuracy mantle convection simulation through modern numerical methods. *Geophysical Journal International*, 191.

Lallemand, S., Heuret, A., and Boutelier, D. (2005). On the relationships between slab dip, back-arc stress, upper plate absolute motion, and crustal nature in subduction zones. *Geochemistry, Geophysics, Geosystems*, 6(9).

Lallemand, S., Peyret, M., Arcay, D., and Heuret, A. (2024). Accretion versus erosion and sediment transfer balance near the subduction interface. *Comptes Rendus. Géoscience*, 356(S2):27–51.

Lamb, S. (2006). Shear stresses on megathrusts: Implications for mountain building behind subduction zones. *Journal of Geophysical Research: Solid Earth*, 111(B7).

Lamb, S. and Davis, P. (2003). Cenozoic climate change as a possible cause for the rise of the Andes. *Nature*, 425(6960):792–797.

Lee, C. and King, S. D. (2011). Dynamic buckling of subducting slabs reconciles geological and geophysical observations. *Earth and Planetary Science Letters*, 312(3-4):360–370.

Liu, L., Gurnis, M., Seton, M., Saleeby, J., Müller, R. D., and Jackson, J. M. (2010). The role of oceanic plateau subduction in the laramide orogeny. *Nature Geoscience*, 3(5):353–357.

MacKay, M. E. and Moore, G. F. (1990). Variation in deformation of the south panama accretionary prism: Response to oblique subduction and trench sediment variation. *Tectonics*, 9(4):683–698.

Massonne, H.-J., Willner, A. P., and Gerya, T. (2007). Densities of metapelitic rocks at high to ultrahigh pressure conditions: What are the geodynamic consequences? *Earth and Planetary Science Letters*, 256(1-2):12–27.

Montheil, L., Philippon, M., Cornée, J.-J., BouDagher-Fadel, M., van Hinsbergen, D. J., Camps,

P., Maffione, M., Audemard, F., Brons, B., Van der Looij, K. J., et al. (2023). Geological architecture and history of the antigua volcano and carbonate platform: Was there an oligo–miocene lull in lesser antilles arc magmatism? *Bulletin*, 135(5-6):1566–1586.

Munch, J., Ueda, K., Schnydrig, S., May, D. A., and Gerya, T. V. (2022). Contrasting influence of sediments vs surface processes on retreating subduction zones dynamics. *Tectonophysics*, 836(April):229410.

Nakakuki, T. and Mura, E. (2013). Dynamics of slab rollback and induced back-arc basin formation. *Earth and Planetary Science Letters*, 361:287–297.

Peacock, S. M. (1996). Thermal and Petrologic Structure of Subduction Zones. In *Subduction*, pages 119–133. American Geophysical Union (AGU).

Philippon, M., Cornée, J.-J., Münch, P., Van Hinsbergen, D. J., BouDagher-Fadel, M., Gailler, L., Boschman, L. M., Quillevere, F., Montheil, L., Gay, A., et al. (2020). Eocene intra-plate shortening responsible for the rise of a faunal pathway in the northeastern caribbean realm. *PLoS One*, 15(10):e0241000.

Pons, M., Sobolev, S. V., Liu, S., and Neuharth, D. (2022). Hindered trench migration due to slab steepening controls the formation of the central andes. *Journal of Geophysical Research: Solid Earth*, 127(12):e2022JB025229.

Pusok, A. E., Stegman, D. R., and Kerr, M. (2022). The effect of low-viscosity sediments on the dynamics and accretionary style of subduction margins. *Solid Earth*, 13(9):1455–1473.

Ribe, N. M. (2003). Periodic folding of viscous sheets. *Physical Review E*, 68(3):036305.

Riedel, M. R. and Karato, S.-i. (1997). Grain-size evolution in subducted oceanic lithosphere associated with the olivine-spinel transformation and its effects on rheology. *Earth and Planetary Science Letters*, 148(1-2):27–43.

Rodríguez-González, J., Billen, M. I., Negredo, A. M., and Montesi, L. G. (2016). Along-strike variation in subducting plate velocity induced by along-strike variation in overriding plate structure: Insights from 3d numerical models. *Journal of Geodynamics*, 100:175–183.

Rodríguez-González, J., Negredo, A. M., and Billen, M. I. (2012). The role of the overriding plate thermal state on slab dip variability and on the occurrence of flat subduction. *Geochemistry,*

Geophysics, Geosystems, 13(1).

Rose, I., Buffett, B., and Heister, T. (2017). Stability and accuracy of free surface time integration in viscous flows. *Physics of the Earth and Planetary Interiors*, 262:90–100.

Ruh, J., Behr, W., and Tokle, L. (2024). Effect of Grain-Size and Textural Weakening in Polyphase Crustal and Mantle Lithospheric Shear Zones. *Tektonika*, 2(1).

Saffer, D. M. and Tobin, H. J. (2011). Hydrogeology and Mechanics of Subduction Zone Forearcs: Fluid Flow and Pore Pressure. *Annual Review of Earth and Planetary Sciences*, 39(Volume 39, 2011):157–186.

Schellart, W. (2010). Evolution of subduction zone curvature and its dependence on the trench velocity and the slab to upper mantle viscosity ratio. *Journal of Geophysical Research: Solid Earth*, 115(B11).

Schellart, W. P. (2024). Subduction dynamics and overriding plate deformation. *Earth-Science Reviews*, 253:104755.

Schellart, W. P., Freeman, J., Stegman, D. R., Moresi, L., and May, D. (2007). Evolution and diversity of subduction zones controlled by slab width. *Nature*, 446(7133):308–311.

Schellart, W. P. and Moresi, L. (2013). A new driving mechanism for backarc extension and backarc shortening through slab sinking induced toroidal and poloidal mantle flow: Results from dynamic subduction models with an overriding plate. *Journal of Geophysical Research: Solid Earth*, 118(6):3221–3248.

Schellart, W. P. and Rawlinson, N. (2013). Global correlations between maximum magnitudes of subduction zone interface thrust earthquakes and physical parameters of subduction zones. *Physics of the Earth and Planetary Interiors*, 225:41–67.

Sobolev, S. V. and Brown, M. (2019). Surface erosion events controlled the evolution of plate tectonics on earth. *Nature*, 570(7759):52–57.

Stegman, D. R., Schellart, W. P., and Freeman, J. (2010). Tectonophysics competing in fl uences of plate width and far- fi eld boundary conditions on trench migration and morphology of subducted slabs in the upper mantle. *Tectonophysics*, 483:46–57. Our current models are the threshold from thin to intermediate width.-Subduction velocities should be similar.-Retreat rate

should increase with width, but less for intermediate+ widths.

Stern, R. J. (2002). Subduction Zones. *Reviews of Geophysics*, 40(4):3–1–3–38.

Stoner, R., Holt, A., Epstein, G., Guevara, V., and Condit, C. (2025). Emergent feedbacks between progressive serpentinization, interface weakening, and subduction rates. *Geochemistry, Geophysics, Geosystems*, 26(11):e2025GC012488.

Suchoy, L., Goes, S., Maunder, B., Garel, F., and Davies, R. (2021). Effects of basal drag on subduction dynamics from 2d numerical models. *Solid Earth*, 12(1):79–93.

Sun, T., Saffer, D., and Ellis, S. (2020). Mechanical and hydrological effects of seamount subduction on megathrust stress and slip. *Nature Geoscience*, 13(3):249–255.

Tobin, H. J. and Saffer, D. M. (2009). Elevated fluid pressure and extreme mechanical weakness of a plate boundary thrust, nankai trough subduction zone. *Geology*, 37(8):679–682.

Tokle, L., Hirth, G., and Behr, W. M. (2019). Flow laws and fabric transitions in wet quartzite. *Earth and Planetary Science Letters*, 505:152–161.

Tokle, L., Hufford, L. J., Behr, W. M., Morales, L. F. G., and Madonna, C. (2023). Diffusion Creep of Sodic Amphibole-Bearing Blueschist Limited by Microboudinage. *Journal of Geophysical Research: Solid Earth*, 128(9):e2023JB026848.

Toth, J. and Gurnis, M. (1998). Dynamics of subduction initiation at preexisting fault zones. *Journal of Geophysical Research: Solid Earth*, 103(B8):18053–18067.

Turino, V. and Holt, A. F. (2024). Spatio-temporal variability in slab temperature within dynamic 3-d subduction models. *Geophysical Journal International*, 236(3):1484–1498.

Underwood, M. B. (2007). Sediment Inputs to Subduction Zones: Why Lithostratigraphy and Clay Mineralogy Matter. In Dixon, T. H. and Moore, C., editors, *The Seismogenic Zone of Subduction Thrust Faults*, pages 42–85. Columbia University Press.

van den Broek, J. M. and Gaina, C. (2020). Microcontinents and continental fragments associated with subduction systems. *Tectonics*, 39(8):e2020TC006063.

van der Wiel, E., Pokornỳ, J., Čížková, H., Spakman, W., van den Berg, A. P., and van Hinsbergen, D. J. (2024). Slab buckling as a driver for rapid oscillations in indian plate motion and subduction rate. *Communications Earth & Environment*, 5(1):316.

van Hunen, J., van den Berg, A. P., and Vlaar, N. J. (2002). On the role of subducting oceanic plateaus in the development of shallow flat subduction. *Tectonophysics*, 352(3):317–333.

Vrolijk, P. (1990). On the mechanical role of smectite in subduction zones. *Geology*, 18(8):703–707.

Zhang, J. and Green, H. W. (2007). Experimental Investigation of Eclogite Rheology and Its Fabrics at High Temperature and Pressure. *Journal of Metamorphic Geology*, 25(2):97–115.

Zhang, J., Green, H. W., and Bozhilov, K. N. (2006). Rheology of omphacite at high temperature and pressure and significance of its lattice preferred orientations. *Earth and Planetary Science Letters*, 246(3):432–443.

Zhong, S. and Gurnis, M. (1994). Controls on trench topography from dynamic models of subducted slabs. *Journal of Geophysical Research: Solid Earth*, 99(B8):15683–15695.

Zhong, S. and Gurnis, M. (1995). Mantle Convection with Plates and Mobile, Faulted Plate Margins. *Science*, 267(5199):838–843.

Zoback, M. L. (1992). First-and second-order patterns of stress in the lithosphere: The world stress map project. *Journal of Geophysical Research: Solid Earth*, 97(B8):11703–11728.

Zuhair, M., Gollapalli, T., Capitanio, F. A., Betts, P. G., and Graciosa, J. C. (2022). The role of slab steps on tectonic loading along subduction zones: Inferences on the seismotectonics of the sunda convergent margin. *Tectonics*, 41(9):e2022TC007242.

This paper has been produced using the Blackwell Scientific Publications GJI LaTeX2e class file.